AGU PUBLICATIONS

JGR

Journal of Geophysical Research: Earth Surface

RESEARCH ARTICLE
10.1002/2015JF003520

Key Points:
- More intense rainfall results in more abundant and larger landslides farther down hollows
- Higher root cohesion results in less abundant and larger landslides restricted to deeper soils
- Model overlaps 65% of observed landslides, predicting 55% of their sizes within a factor of 2

Correspondence to:
D. Bellugi,
dinob@mit.edu

Citation:
Bellugi, D., D. G. Milledge, W. E. Dietrich, J. T. Perron, and J. McKean (2015), Predicting shallow landslide size and location across a natural landscape: Application of a spectral clustering search algorithm, *J. Geophys. Res. Earth Surf.*, *120*, 2552–2585, doi:10.1002/2015JF003520.

Received 2 MAR 2015
Accepted 4 NOV 2015
Accepted article online 9 NOV 2015
Published online 22 DEC 2015

Predicting shallow landslide size and location across a natural landscape: Application of a spectral clustering search algorithm

Dino Bellugi[1], David G. Milledge[2], William E. Dietrich[3], J. Taylor Perron[1], and Jim McKean[4]

[1]Department of Earth, Atmospheric, and Planetary Sciences, Massachusetts Institute of Technology, Cambridge, Massachusetts, USA, [2]Department of Geography, Durham University, Durham, UK, [3]Department of Earth and Planetary Science, University of California, Berkeley, California, USA, [4]U.S. Forest Service, Rocky Mountain Research Station, U.S. Department of Agriculture, Boise, Idaho, USA

Abstract Predicting shallow landslide size and location across landscapes is important for understanding landscape form and evolution and for hazard identification. We test a recently developed model that couples a search algorithm with 3-D slope stability analysis that predicts these two key attributes in an intensively studied landscape with a 10 year landslide inventory. We use process-based submodels to estimate soil depth, root strength, and pore pressure for a sequence of landslide-triggering rainstorms. We parameterize submodels with field measurements independently of the slope stability model, without calibrating predictions to observations. The model generally reproduces observed landslide size and location distributions, overlaps 65% of observed landslides, and of these predicts size to within factors of 2 and 1.5 in 55% and 28% of cases, respectively. Five percent of the landscape is predicted unstable, compared to 2% recorded landslide area. Missed landslides are not due to the search algorithm but to the formulation and parameterization of the slope stability model and inaccuracy of observed landslide maps. Our model does not improve location prediction relative to infinite-slope methods but predicts landslide size, improves process representation, and reduces reliance on effective parameters. Increasing rainfall intensity or root cohesion generally increases landslide size and shifts locations down hollow axes, while increasing cohesion restricts unstable locations to areas with deepest soils. Our findings suggest that shallow landslide abundance, location, and size are ultimately controlled by covarying topographic, material, and hydrologic properties. Estimating the spatiotemporal patterns of root strength, pore pressure, and soil depth across a landscape may be the greatest remaining challenge.

1. Introduction

Mechanistic models share common elements for predicting shallow landslides (involving only the colluvial soil mantle) across a landscape. They divide the landscape into cells (of fixed or variable size); they assign or calculate properties important to slope stability, such as soil depth and pore water pressure, for each cell; they then commonly calculate the stability of each cell independently using a one-dimensional (infinite-slope) limit equilibrium stability model [e.g., *Montgomery and Dietrich*, 1994; *Dietrich et al.*, 1995; *Wu and Sidle*, 1995; *Pack et al.*, 1998; *Iverson*, 2000; *Dietrich et al.*, 2001; *Dhakal and Sidle*, 2003; *Rosso et al.*, 2006; *Godt et al.*, 2008]. These models predict landslide location or susceptibility (i.e., the potential for landsliding at a location). They define landslide dimensions implicitly either by the grid cell size or by the size of groups of adjacent unstable cells (whose instability is independently calculated), which they assume fail together, rather than by any explicit prediction. This approach is strongly dependent on the grid cell size [*Dietrich et al.*, 2001; *Claessens et al.*, 2005] and cannot accurately estimate the size of individual shallow landslides [*Dietrich et al.*, 2007; *Anagnostopoulos et al.*, 2015]. Because the size of a shallow landslide strongly influences both its hazard potential and geomorphic effects, this is a major shortcoming [e.g., *Benda and Cundy*, 1990; *Fannin and Wise*, 2001; *Hungr et al.*, 2008]. A one-dimensional treatment of stability also affects which locations are potentially unstable and the rainfall required to trigger failure by neglecting the stabilizing effect of lateral resistance. The inability of such models to predict discrete individual landslides also limits our understanding of the controls of factors such as rainfall intensity or root strength on landslide location and size.

Observations (and the existence of empirical rainfall thresholds) consistently show that landslides are more abundant with increased rainfall amount (intensity and/or duration) (e.g., review in *Sidle and Ochiai* [2006]).

Similarly, the effects of logging, fire, land use change, and their associated reduction in root cohesion have been shown to exert a strong influence on the abundance of landslides in many locations (e.g., review in *Sidle and Ochiai* [2006]). Investigations of landslide size for different vegetation types suggest that forest and shrubland areas where plants have stronger or denser root systems often result in generally larger landslides [*Moser*, 1971; *Rice and Foggin*, 1971; *Selby*, 1976; *Lehre*, 1982; *Reneau and Dietrich*, 1987a; *Moser and Schoger*, 1989; *Gabet and Dunne*, 2003; *Rickli and Graf*, 2009]. The location of landslides also changes with vegetation type. *Gabet and Dunne* [2003] found low root strength failures on gentler slopes, although this could be due to preferential conversion of gentler slopes to grassland. In areas that were not converted to grassland they find an inverse relation between slope and landslide volume and attribute it to the effects of lateral reinforcement; no such trend is found in grassland. Several other studies suggest that landslides in forested areas occurred on steeper slopes than those in unforested areas [*Moser and Schoger*, 1989; *Rickli and Graf*, 2009]. *Rickli and Graf* [2009] suggest that root reinforcement is the main reason for this shift.

Observations on landslide size and location for different rainfall intensities are, to our knowledge, much more limited. *Wieczorek* [1987] found that long-duration, moderate-intensity storms triggered debris flows on moderate slopes in convergent topography, while short-duration high-intensity storms can trigger landslides on steep planar hillsides. *Larsen and Simon* [1993] found that short-duration, high-intensity rainfall events generally result in shallow soil slips and debris flows, while long-duration, low-intensity rainfall generally produces larger, deeper debris avalanches and slumps. *Saito et al*. [2014] found that in Japan larger landslides were more abundant at the expense of smaller ones when total, maximum, and mean rainfall intensity exceeded specific thresholds.

In order to enable the prediction of shallow landslide size and location, *Bellugi et al*. [2015] developed an efficient search algorithm to identify clusters of adjacent grid cells that fail as discrete landslides. This algorithm does not impose constraints on landslide size or shape, besides those imposed by the grid discretization (e.g., landslides cannot be smaller than a single grid cell, and their boundaries must coincide with the grid cell boundaries). Using this search algorithm, they were able to predict the size and location of a shallow landslide at an instrumented field site using field-measured physical parameters.

In this paper, we apply their method to a larger natural landscape (~0.5 km^2), where the physical parameters are less well constrained. This is challenging because properties relevant to landsliding, such as soil depth and pore water pressure, are variable in space and time and are difficult to measure across a landscape at a suitable resolution. We therefore combine the model of *Bellugi et al*. [2015] with simple submodels that exploit the topographic control on soil depth and pore water pressure to predict shallow landslide size and location across a landscape. We test our model, in a landslide-prone study area near the Mettman Ridge in the Oregon Coast Range (CB-MR), USA, where a decade-long inventory of rainfall-triggered shallow landslides is available and fieldwork has constrained soil hydrological and mechanical properties [e.g., *Torres et al*., 1998; *Schmidt*, 1999; *Montgomery et al*., 2000; *Schmidt et al*., 2001; *Montgomery and Dietrich*, 2004; *Ebel et al*., 2007a, 2007b; *Montgomery et al*., 2009]. Our goal is to explore the usefulness of our approach in a practical application to a landscape where detailed conditions are not known and to quantify the impacts of changes in rainfall and root strength on landslide size and location.

We use process-based submodels with field-based measurements to find the best estimates of each model parameter (the base case parameterization) to map soil depth and predict the pore pressure and root strength fields. We then use the inventory of observed landslides as an independent test of the model rather than calibrating any model parameters to optimize model performance. This more stringent test illustrates the model's applicability for forward predictions where landslide model parameters are unknown. Given the large uncertainty about parameters, model performance under a range of parameters is also explored. A range of performance metrics is used to assess improvement relative to the null hypothesis that landslides are randomly placed on the landscape (referred to as the random model), and common infinite-slope approaches (e.g., review in *Sidle and Ochiai* [2006]). We independently test the search algorithm and slope stability model by (1) assessing the predicted stability of the observed landslides using the slope stability model alone, under various parameterizations; and (2) confirming that any observed landslide that is unstable according to the slope stability model is also found by the search algorithm. Finally, we apply the model to the same study area with the same base case parameterization but vary rainfall intensity and root strength to understand their impact on landslide location and size.

2. Background

2.1. Discrete Landslide Modeling Approaches

Physically based modeling of shallow landslide size requires a multidimensional slope stability model that can be applied efficiently across a landscape and use information at the individual grid cell level to assess collective cell instability without constraints on size and shape. Because of the geomechanical complexity of natural landscapes, there have been few attempts to develop such a model. Previous efforts to model discrete landslides fall into two general categories: limit equilibrium analyses that constrain the number of potential failures to test and models of progressive failure that constrain the number of initiation points.

Okimura [1994] identified a least stable grid cell using an infinite-slope model and assumed failure depth; then calculated a more complete cross-slope and downslope force equilibrium to identify the least stable location in a set of predefined rectangular shapes in its neighborhood. This model was successfully applied to small individual failure sites but was sensitive to grid resolution and too restrictive for larger scale applications. *Qiu et al*. [2007] used a model proposed by *Xie et al*. [2003], which combines a nondeterministic Monte Carlo approach with a 3-D slope stability method [*Hovland*, 1977], to test the stability of potential ellipsoidal slip surfaces. The random variables (the dimensions and the dip angle of the ellipsoid) are sampled from a uniform distribution within user-specified ranges. This approach also does not consider resistance on the margins due to, for example, lateral root reinforcement, which we expect to be important [*Schmidt et al*., 2001]. *Mergili et al*. [2014] extended the same method to also predict deep-seated landslides and report a modest improvement on the infinite-slope model. *Reid et al*. [2000] and *Brien and Reid* [2008] take a similar approach to *Xie et al*. [2003] but use a deterministic sampling strategy in order to predict deep-seated landslides. The candidate landslides are the result of the intersection of the topographic surface and a prescribed set of spheres of given radii, and their stability is assessed using Bishop's 3-D slope stability method [*Bishop*, 1955] (also ignoring lateral resistance).

Lehmann and Or [2012] described a hillslope as discretized soil columns interconnected by frictional and tensile mechanical bonds represented as fiber bundles [e.g., *Schwarz et al*., 2010]. If a failure threshold is reached based on the forces acting on the base of a column, its load is redistributed to its neighbors via the fiber bundles, which in turn can gradually fail, allowing the failure to progress in both the upslope and downslope directions. The model of *Lehmann and Or* [2012] acknowledges the progressive nature of many failures and produces power law size frequency scaling compatible with many landslide inventories [e.g., *Stark and Hovius*, 2001; *Guzzetti et al*., 2002; *Malamud et al*., 2004]. However, it is computationally intensive and as a result has only been applied to small synthetic landscapes. To predict the size, location, and timing of landslides over larger landscapes, *Von Ruette et al*. [2013] simplified the *Lehmann and Or* [2012] model by connecting adjacent columns with prescribed brittle mechanical bonds rather than the fiber bundles. When applied to two catchments (3–4 km^2) in the foothills of the Swiss Alps, it generally reproduced the size of observed landslides but predicted failures only at much steeper slopes than observed. Both models implicitly assume that deformation is large enough to allow failure at the base of an element and subsequent tensile cracking upslope, yet small enough to allow the transfer of the loads through columns leaning on their downslope neighbors. The approach of *Bellugi et al*. [2015], which we describe in sections 3 and 4, uses a more conventional limit equilibrium analysis [*Milledge et al*., 2014] paired with a novel search algorithm. We contrast this approach applied to our study area with those of *Qiu et al*. [2007], *Mergili et al*. [2014], and *Von Ruette et al*. [2013] in section 7.2.1.

2.2. Parameterization

Slope stability models require parameterization of many attributes that can vary in space and time. All models depend strongly on local slope and drainage area and thus on topographic resolution [*Zhang and Montgomery*, 1994; *Dietrich et al*., 2001]. In most models, soil density, cohesion, and friction angle have been determined by laboratory tests and kept spatially constant across the landscape [e.g., *Montgomery and Dietrich*, 1994; *Rosso et al*., 2006; *Godt et al*., 2008; *Simoni et al*., 2008]. Soil depth is either assumed uniform [e.g., *Montgomery et al*., 2000; *Mergili et al*., 2014], predicted empirically [e.g., *Godt et al*., 2008], inferred from mapping units [e.g., *Wu and Sidle*, 1995], or predicted using a mechanistic model [e.g., *Dietrich et al*., 1995; *Von Ruette et al*., 2013]. Root strength varies spatially and temporally across a landscape due to land management [*Montgomery et al*., 2000; *Dhakal and Sidle*, 2003; *Sidle and Ochiai*, 2006], as well as natural variability in vegetation type, and the distribution and strength of its roots [*Schmidt et al*., 2001; *Dhakal and Sidle*, 2003; *Hales et al*., 2009].

Existing shallow landslide models are primarily differentiated by their method of estimating pore water pressure. The two dominant mechanisms that generate high pore water pressures are topographically steered subsurface flow, over hours to weeks, and rapid vertical infiltration, over minutes to hours [*Iverson*, 2000]. Models range from short-timescale vertical flux dominated [e.g., *Iverson*, 2000; *Godt et al*., 2008], to longer-timescale lateral flux dominated [e.g., *Montgomery and Dietrich*, 1994; *Wu and Sidle*, 1995], with some models accounting for both but at considerable computational cost [e.g., *Simoni et al*., 2008]. Modeling the longer-term lateral component by assuming steady state conditions is attractive for its simplicity but does not capture transient pore water pressure development. Other models include this transient behavior while retaining relative simplicity by relaxing the steady state assumption [e.g., *Iida*, 1984; *Wu and Sidle*, 1995; *Borga et al*., 2002; *Rosso et al*., 2006]. Transient, variably saturated, and fully three-dimensional models have been used at the scale of individual landslide sites [e.g., *Wilson et al*., 1989; *Ebel et al*., 2007a, 2007b] but are too computationally demanding to apply across larger watersheds. Furthermore, local pore pressures may be controlled by local heterogeneities in the material properties, for example, exfiltration of water from underlying fractured bedrock, such that computationally demanding pore pressure models cannot be sufficiently parameterized due to lack of knowledge of the subsurface [e.g., *Montgomery et al*., 1997; *Ebel et al*., 2007a, 2007b; *Sidle and Chigira*, 2004]. Given these challenges, in this study we adopt a simplified process-based model for pore pressure dynamics that balances ease of computation with the ability to include transient hydrologic effects.

2.3. Metrics for Evaluating Landslide Model Performance

To be useful, a model must at least improve on the random model case but should also improve on previous models in specific applications. Model evaluation should assess (1) the adequacy (conceptual and mathematical) of the model at describing the system, (2) the agreement between predictions and observations, and (3) the model's robustness to small changes in the input data [*Frattini et al*., 2010]. Typically, landslide model performance assessments assume model adequacy; they generally test agreement and occasionally test robustness. Any model test requires decisions on (1) how to compare predicted and observed landslides and (2) the degree of model parameter calibration allowed for the model to reproduce the observations. Calibration is necessary where model parameters represent properties that are difficult or impossible to measure but may result in unreasonable performance estimates if the same observations are used both for calibration and assessment.

Strictly, agreement represents the degree to which predicted and observed landslides have the same size and shape, occur in the same location, and at the right time (e.g., CB-1 test in *Bellugi et al*. [2015]). However, few models are capable of predicting discrete landslides, and incomplete knowledge of local conditions makes it unlikely that the exact timing, size, and location of a specific landslide could effectively be predicted by any model at the landscape scale. In practice, the agreement test is generally relaxed to compare (1) the percentage of observed landslides that are captured (i.e., overlapped by a predicted landslide), either by number [e.g., *Dietrich et al*., 2001] or by area [e.g., *Mergili et al*., 2014], and the percentage of the landscape predicted as unstable [e.g., *Dietrich et al*., 2001]; (2) the similarity in predicted and observed landslide size distributions [e.g., *Stark and Guzzetti*, 2009] or in some bulk index of location in the landscape [e.g., *Von Ruette et al*., 2013].

Such tests often relate true positives (TP) or negatives (TN), where landslide presence or absence is correctly predicted, to false positives or negatives, where a landslide is either predicted without occurring (FP) or occurred but was not predicted (FN) [*Van Rijsbergen*, 1979; *Frattini et al*., 2010; *Bellugi*, 2012]. These classes can be combined to indicate the probabilities that any given location is correctly labeled (accuracy = (TP + TN)/(TP + TN + FP + FN)), that a predicted landslide is indeed a landslide (precision = TP/(TP + FP)), or that an observed landslide is predicted (recall = TP/(TP + FN), also known as the true positive rate). These metrics are generally combined into Receiver Operating Characteristic (ROC) or success rate (SR) curves to assess the model's ability to predict observed landslides, without misclassifying a large part of the landscape [*Corominas et al*., 2014]. The ROC curve relates the true positive rate to the false positive rate (FP/(FP + TN)), while the SR curve relates the true positive rate to the total proportion of the landscape predicted as a landslide ((TP + FP)/(TP + FP + TN + FN)) [*Chung and Fabbri*, 2003]. These curves are not overly sensitive to the number of observed landslides [*Fawcett*, 2006] and are independent of the cutoff between precision and recall, since the area under the curve reflects the performance of the model over the range of possible cutoffs [*Hanley and McNeil*, 1982].

Both curves can be trivially compared to random predictions, which follow the 1:1 line [*Beguería*, 2006]. These calculations require a complete inventory of real landslides, which is very difficult to obtain.

Incomplete knowledge of local conditions inhibits the accuracy of landslide models for a specific event [e.g., *Montgomery and Dietrich*, 1994; *Dietrich et al*., 2001; *Van Westen et al*., 2006]. These problems can be overcome to some extent by comparing landslide predictions with observations over a much longer time period, but this is limited by the lack of long-term observational landslide records, preventing a fair estimate of both FNs and FPs. For example, a FP can be a genuine error, a real hazard-prone area that has not yet developed into a landslide, or an area where the landslide already occurred (preventing one from occurring in the study period) [*Beguería*, 2006]. In general, any additional landslide occurring outside the observation period would either transform a TN into a FN or FP into a TP. Thus, we also consider the model's ability to reproduce landslide size and location more generally, by comparing the probability density functions (PDF) of landslide size and of location (as represented by a topographic index). This comparison is less sensitive to the accuracy and completeness of the observational set.

The uncalibrated performance of the model is evaluated by comparing the percentage of correctly predicted landslides to the percentage of the landscape predicted as unstable. These values are compared to those of an infinite-slope model using an identical parameterization and the random model null hypothesis is tested by comparing the model's agreement with observed landslides to that with landslides randomly placed on the landscape. We compare PDFs of predicted and observed landslide size and location. Given the inevitable uncertainty in model parameters, the impact of different parameterizations on performance is explored using SR curves, which are compared to a random model and the infinite-slope model. This allows gauging the robustness of our model to variations in some of the model parameters.

3. Slope Stability Model

Although shallow landslides commonly transform into debris flows, we propose that the initial failure may be represented by a rigid block failure model. The multidimensional stability model MD-STAB described by *Milledge et al*. [2014] is adopted in this study, as it is appropriate for shallow landslide modeling across natural landscapes, is fully three dimensional, and incorporates the effects of root strength and soil friction on sloping boundaries. Other models that make the block failure assumption could also be used with the search algorithm to identify landslide location and size (section 4).

Milledge et al. [2014] discretize the landscape into columns extending from the ground surface to the bedrock interface and compute the stability of groups of adjacent columns using a framework similar to *Hovland*'s [1977] limit equilibrium method. The factor of safety (FS) is defined as the ratio of total resisting force to total driving force along the failure surface. Resisting forces result from friction and root cohesion on the base, cross-slope sides, upslope, and downslope margins of the group of columns, while driving forces result from the downslope component of each column's weight and the force exerted from the soil mass upslope.

Failure is assumed to occur by simultaneous shear on the boundaries of the landslide without internal deformation, progressive failure, strain weakening, or strain-induced pore water pressure dynamics. It is assumed that the soils are normally consolidated, cohesionless, have isotropic frictional properties, and are uniform in density for all soil moisture conditions [*Milledge et al*., 2014]. Soil cohesion can also be included in the model when appropriate. It is also assumed that slope instability occurs in drained conditions (i.e., strain rates are slower than the rate at which water can drain from the soil, resulting in no pore pressure increase [*Head and Epps*, 2014]); that the failure plane is at the soil-bedrock interface; that the water table surface in a soil column is parallel to both the ground surface and the base of the soil; and that groundwater conditions are the result of steady, slope-parallel subsurface flow. For simplicity, the effects of infiltration, suction, or capillary rise in the unsaturated zone that might cause negative pore pressures are ignored, and each column is represented with saturated and unsaturated zones. However, other groundwater assumptions could also be used to predict a pore water pressure field for the slope stability model.

The basal shear resistance force R_b (N) is

$$R_b = (\sec\theta C_b + \cos\theta z(\gamma_s - \gamma_w m)\tan\phi)lw \quad (1)$$

where l (m) and w (m) are the length and width of each cell, θ (deg) is the slope angle, ϕ (deg) is the soil's effective friction angle, m (no unit) is the soil saturation ratio (the ratio of water table height h (m) to the

depth of the failure plane z (m)), γ_s is the unit weight of the soil, defined as $\gamma_s = g\ \rho_s$ (N/m^3), γ_w is the unit weight of water, defined as $\gamma_w = g\ \rho_w$ (N/m^3), g (m/s^2) is acceleration due to gravity, ρ_s (kg/m^3) is the soil bulk density, ρ_w (kg/m^3) is the density of water, and C_b (Pa) is the effective basal root cohesion.

The cross-slope shear resistance forces R_l and R_r (N) are

$$R_l = R_r = \frac{1}{2} K_o z^2 \left(\gamma_s - \gamma_w m^2\right) \tan\phi l + C_l z l \tag{2}$$

where friction is a function of the normal stress on the margin calculated using the at-rest earth pressure coefficient, defined as $K_0 = 1 - \sin\ \phi$ [*Jaky*, 1944].

The forces acting on the upslope and downslope margins are the resultant of both the normal and shear forces (due to friction) and are inclined at the soil friction angle (ϕ). Their slope-parallel component acts as a driving or resisting force on the margin, while their slope-normal component modifies the resisting force on the base. The active force on the upslope margin of the group of columns is calculated from vertical stress using the Coulomb active earth pressure coefficient (K_a), which assumes a planar failure surface [*Chugh and Smart*, 1981]. The passive force on the downslope margin is calculated using the Log-Spiral passive earth pressure coefficient (K_p), which accounts for the curvature of the failure surface that develops on this margin [*Soubra and Macuh*, 2002]. Both are upper bound solutions suitable for sloping soils that account for root cohesion. The net resisting force on the passive downslope margin R_d (N) is

$$R_d = \frac{1}{2} K_p z^2 \left(\gamma_s - \gamma_w m^2\right) w(\cos(\phi - \theta) - \sin(\phi - \theta)\tan\phi) \tag{3}$$

The net driving force on the active upslope margin R_u (N) is

$$R_u = \frac{1}{2} K_a z^2 \left(\gamma_s - \gamma_w m^2\right) w(\cos(\phi - \theta) - \sin(\phi - \theta)\tan\phi) \tag{4}$$

R_u becomes negative when cohesion is large enough to exceed the driving force of the upslope wedge. The downslope driving force F_d (N) is defined as

$$F_d = \sin\theta z \gamma_s l w \tag{5}$$

Milledge et al. [2014] calculate the driving force vector (equation (5)) for each column based on its aspect, then sum these vectors over the entire landslide area to obtain the total driving force. The resisting force of each column is the sum of its basal (equation (1)) and lateral components (equations (2)–(4)). Lateral components are only considered for column margins at the edge of the landslide. As grids are generally not oriented parallel to the topographic gradient, most cells will experience more than one force component (upslope, downslope, and cross slope). The lateral resistance on each column margin is adjusted by assigning a fraction of the edge length to each resistance component. The FS (no unit) for the group of columns is defined as the ratio of its total resisting to driving forces,

$$\mathrm{FS} = \frac{\sum_{\text{all}} R_b + \sum_{\text{left}} R_l + \sum_{\text{right}} R_r + \sum_{\text{down}} R_d - \sum_{\text{up}} R_u}{\sum_{\text{all}} F_d} \tag{6}$$

where the summation subscripts indicate which columns are included (all columns or only those on the left, right, downslope, or upslope margins). An extensive derivation and discussion of this model is provided in *Milledge et al*. [2014].

4. Search Algorithm

To identify discrete landslides in the output of the slope stability model, we use the search algorithm based on graph-partitioning theory developed by *Bellugi et al*. [2015]. Here the search algorithm is summarized, abstracted from the more extensive derivation, and discussed in *Bellugi et al*. [2015]. The landscape and all its spatial attributes are discretized into a regular grid and represented as an undirected weighted graph $G = (V,E)$. The vertices $v \in V$ represent the vertical soil columns corresponding to the discretized grid cells in the slope stability model. An edge $e_{ij} \in E$ is formed between every pair of neighboring vertices v_i and v_j representing the forces w_{ij} acting between grid cells. The vertices are annotated with the gravitational

driving forces and the frictional resistive forces acting on the base of the column, contributed by each grid cell. The edges are annotated with the forces potentially acting between a grid cell and its neighbors. The aim is to find unstable clusters of vertices with a ratio of resistive to driving forces (FS) less than unity. This is achieved by expressing the FS as a cost function, minimizing it over the graph, then relaxing the least stable criterion to include any unstable clusters [*Bellugi et al.*, 2015].

Bellugi et al. [2015] define a force matrix **F** containing the driving forces associated with the vertices of *G*,

$$\mathrm{F}_{ii} = F_{d_i} \tag{7}$$

where F_{d_i} is the force contributed by vertex v_i. For efficiency, only the magnitude of the driving force (the arithmetic sum of the driving forces on the vertices of a cell) is encoded in **F**. The FS of candidate landslides is subsequently computed using the vector sum. A resistance matrix **R** is defined to express the resistive forces associated with both the vertices and the edges of *G*. The diagonal of **R** is

$$\mathrm{R}_{\mathrm{ii}} = R_{b_i} + \sum_{i \neq j}^{m*n} w_{ij} \tag{8}$$

where R_{b_i} is the basal resistance of vertex v_i, and the second term is the sum of the lateral resistance between v_i and its neighbors. The off-diagonal entries of **R** contain the symmetrized resistive forces along a given edge between v_i and a neighbor v_j:

$$\mathrm{R}_{ij} = \mathrm{R}_{ji} = -\frac{w_{ij} + w_{ji}}{2}, i \neq j \tag{9}$$

A cluster of cells $S \in G$ is defined by a binary indicator vector **x** of length $n*m$: $\mathbf{x}_k = 1$ if $v_k \in S$, and $\mathbf{x}_k = 0$ if $v_k \notin S$. The index k corresponds to the position of a grid cell in a linearized representation of the grid. The cost function $C(\mathbf{x})$ of the partition S is defined as the FS of S expressed in terms of **x**, **R,** and **F**:

$$C(\mathbf{x}) = \frac{\mathbf{x}^T \mathbf{R} \mathbf{x}}{\mathbf{x}^T F \mathbf{x}} \tag{10}$$

The partition S^* with the lowest FS corresponds to the indicator vector $\mathbf{x}^*$ which minimizes $C(\mathbf{x})$ (i.e., $\mathbf{x}^*$ identifies the cluster of cells that minimize the FS). Similarly to the approach of *Shi and Malik* [2000], the binary vector **x** is relaxed to take on real values (i.e., $\mathbf{x} \in \mathbb{R}$). Substituting $\mathbf{y} = \mathbf{F}^{1/2}\mathbf{x}$ into equation (10) leads to

$$C(\mathbf{y}) = \frac{\mathbf{y}^{\mathrm{T}} \mathbf{F}^{-1/2} \mathbf{R} \mathbf{F}^{-1/2} \mathbf{y}}{\mathbf{y}^T \mathbf{y}} \tag{11}$$

The minimizing solution to equation (11) is the eigenvector $\mathbf{y}^*$, pointed to by the smallest nonzero eigenvalue λ^* of the linear system defined by

$$\mathbf{F}^{-1/2} \mathbf{R} \mathbf{F}^{-1/2} \mathbf{y} \;=\; \lambda \mathbf{y} \tag{12}$$

[*Horn, and Johnson*, 1985], where **y** and λ are the eigenvectors and eigenvalues of (12). The partition S^* is obtained by reversing the change of variable used above (i.e., $\mathbf{x}^* = \mathbf{F}^{-1/2}\mathbf{y}^*$). As $\mathbf{x}^*$ is only an approximation of the original discrete **x**, this process is repeated using the first k eigenvectors of equation (12).

Discrete solutions are recovered by thresholding $\mathbf{x}^*$, using all its distinct values. All $\mathbf{x_i}$ for which the corresponding $\mathbf{x_i}^*$ are greater than t_i are set to 1, and the rest are set to 0, producing disconnected discrete binary regions r_i. The set of these regions corresponds to a contour tree T_c, where vertices indicate a topologic change (birth or merging of regions) and edges indicate a change in region shape [*Carr et al.*, 2003]. Each edge of T_c is traversed, and the FS of the region r_i at each threshold t_i is computed using the vector sum of driving forces contributed by each grid cell in the region. Where multiple shapes have a FS below unity, the search algorithm has the option of retaining that with the lowest FS or that with the FS closest to unity [*Bellugi et al.*, 2015]. The former method, referred to as $\mathrm{FS_{min}}$, is most consistent with the form of the optimization (i.e., minimizing the FS), while the latter, referred to as $\mathrm{FS_{max}}$, is more representative of the transition to instability. The process is repeated for the complement of $\mathbf{x}^*$ ($\mathbf{x}^{*\prime} = -\mathbf{x}^*$), whereby all $\mathbf{x_i}$ for which the corresponding $\mathbf{x_i}^*$ are $\leq t_i$ are set to 1, and the rest are set to 0. The set of all the extracted regions represents the predicted landslides from the eigenvector $\mathbf{y}^*$. This process is repeated for each of the k eigenvectors

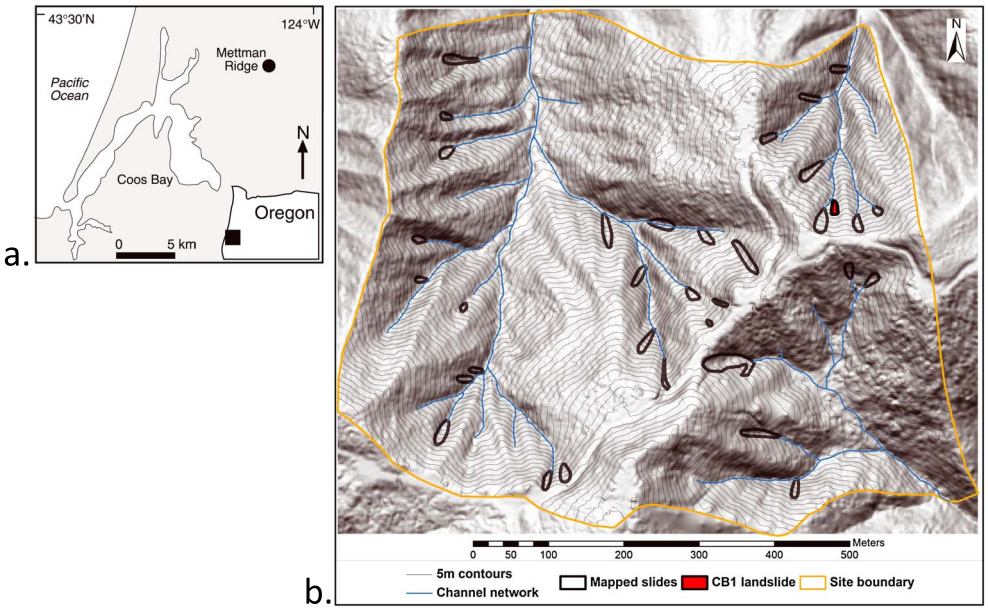

Figure 1. The Coos Bay, OR, study site. (a) Location map showing location of the Mettman Ridge study area near Coos Bay, Oregon [*Montgomery and Dietrich*, 2002]. (b) LiDAR-derived shaded relief map of the Mettman Ridge study area, overlaid with 5 m contours, the channel network, and the landslides mapped by *Montgomery et al*. [2000]. The November 1996 landslide which occurred at the experimental CB-1 site is filled in red.

($k = 256$ in this study, a compromise between fast running times and more exhaustive search). Only one landslide is retained per edge of T_c. Where multiple landslide predictions from different eigenvectors overlap, only one is retained using the same pruning method as above (FS_{min} or FS_{max}).

5. Study Area

The study area (CB-MR) is located about 15 km north of Coos Bay, Oregon (Figure 1a). It has an area of 0.5 km^2 and consists of steep, highly dissected soil-mantled hillslopes with narrow ridges and steep channels typical of the Oregon Coast Range [*Montgomery and Dietrich*, 1994; *Montgomery et al*., 2009]. The maritime climate delivers approximately 1500 mm of annual precipitation [*Montgomery and Dietrich*, 1994; *Montgomery et al*., 2009]. The CB-MR area burned in the late 19th century, was clear-cut logged in 1987, and was replanted in 1988 with Douglas fir seedlings [*Montgomery et al*., 2000, 2009]. In particular, root degradation and hydrological effects following forest clearing resulted in accelerated rates of landsliding [*Montgomery et al*., 2000]. CB-MR is mostly underlain by Eocene sandstone, and the resulting colluvial soils are well mixed, gravelly sands with sandstone clasts [*Torres et al*., 1998; *Schmidt et al*., 2001]. Soil thickness ranges from roughly 0.1 m to 0.5 m on topographic noses to greater than 2 m in topographic hollows, with bedrock outcrops in many areas where the slope exceeds 45° [*Montgomery and Dietrich*, 1994]. The colluvium has a friction angle of 40° and is essentially cohesionless [*Schmidt et al*., 2001]. Roots produce an apparent cohesion via root fiber reinforcement (referred to as root cohesion), promoting slope stability in shallow soils [e.g., *Wu et al*., 1979, 1988; *Sidle*, 1992; *Schmidt et al*., 2001]. Field-mapped channels [*Montgomery and Dietrich*, 1992, 1994] often begin at small landslide scars [*Montgomery and Dietrich*, 1998], and shallow debris flows periodically deliver the colluvial soils to the downslope channel system and scour the bedrock, etching the channel network [*Stock and Dietrich*, 2003]. The average slope of the study area is 36°, with maximum slopes exceeding 60° in some locations.

This site was selected to test our model because (1) repeat field mapping provides an inventory of shallow landslides that occurred over a 10 year period [*Montgomery et al*., 2000] and (2) various campaigns during this 10 year period produced field measurements of physical parameters such as hydrological conditions, soil depth, and root strength. These measurements include an instrumental record of a rainfall-triggered shallow landslide that occurred in a small catchment (CB-1) at the research site [*Montgomery et al*., 2009] as well as measurements over a larger area of soil depth [*Schmidt*, 1999; *Heimsath et al*., 2001], root strength [*Schmidt et al*., 2001; *Montgomery et al*., 2009], hydrological properties [*Torres et al*., 1998; *Montgomery and Dietrich*, 2004;

Ebel et al., 2007a, 2007b], and rainfall characteristics [*Montgomery et al*., 2000]. These provided a basis for models of soil production [*Heimsath et al*., 2001] and transport [*Roering et al*., 1999], which make it possible to predict the spatial pattern of soil depth [*Dietrich et al*., 1995, 2003]. Given the volume and quality of the data from this site, it has been a benchmark for many landslide models [e.g., *Montgomery and Dietrich*, 1994; *Rosso et al*., 2006; *Borja and White*, 2010].

The 34 shallow landslides that occurred in CB-MR during the decade of research were mapped by *Montgomery et al*. [2000] (Figure 1b). In November 1996 a rainstorm delivered the largest recorded 24 h rainfall to the Oregon Coast Range, triggering widespread landslides [*Robison et al*., 1999]. Between 16 and 18 November, the rain gauges at CB-1 measured 225 mm of rain [*Montgomery et al*., 2009]. The maximum daily intensity was 145 mm/d and the 48 h average intensity was 85 mm/d [*Montgomery et al*., 2009]. About 1 h after the peak rainfall, the slope failed at the CB-1. The colluvium from the CB-1 hollow mobilized as a debris flow, destroying most of the infrastructure at the experimental site and marking the end of the recorded rainfall time series.

6. Application of the Discrete Landslide Model

The model is applied to the 0.5 km^2 study area (CB-MR) to assess its ability to reproduce the size and location of observed landslides. These landslides occurred over a 10 year period and, with the exception of the 1996 storm, the characteristics (i.e., intensity, duration, and detailed time series) of the landslide-triggering storms are poorly known. We adopt the estimates of *Montgomery et al*. [2000] for the characteristics of the storms that triggered landslides. The topographic data consist of a 2 m resolution grid containing LiDAR-derived elevations with an original average data point spacing of 2.3 m [*Roering et al*., 1999]. In contrast with the CB-1 monitoring study [*Bellugi et al*., 2015], soil depth, water table height, and lateral and basal root cohesion at the time of failure are unknown and must instead be estimated from process-based submodels described in the following section.

6.1. Modeling Spatially Variable Soil Properties and Hydrologic Conditions

6.1.1. Soil Properties

Based on the framework illustrated in *Dietrich et al*. [1995], soil depth is estimated by coupling an exponential soil production term [*Heimsath et al*., 2001] with a nonlinear diffusive term [*Roering et al*., 1999] in a finite-difference scheme, which is then run for 6000 years (with a 1 year time step) to match the field observations reported by *Montgomery* [1991]. The rate of conversion of intact bedrock to mobile soil (typically due to biotic disturbance) declines exponentially with soil depth and can be expressed as

$$-\frac{\partial z_b}{\partial t} = \varepsilon e^{-\alpha z \cos\theta} \tag{13}$$

where z_b (m) is the height of the soil bedrock boundary above some datum, t (year) is time, ε (m/yr) is the production rate at zero soil thickness, α (1/m) is the rate constant, z (m) is the soil thickness measured vertically from the bedrock boundary, and θ (deg) is the slope angle. The annual transport across the entire hillslope is determined by the nonlinear flux equation,

$$\mathbf{q} = \frac{D\nabla z_t}{1 - (|\nabla z_t|/S_c)^2} \tag{14}$$

where $\mathbf{q}$ (m^2/yr) is the flux per unit contour width, D (m^2/yr) is the diffusion coefficient, z_t (m) is the topographic elevation above a reference datum, and S_c (m/m) is the critical slope. We use locally calibrated parameters: D is set to 0.0032 (m^2/yr) and S_c to 1.25 (m/m) [*Roering et al*., 1999]; α is set to 0.0003 (1/m) and ε to 0.000268 (m/yr) [*Heimsath et al*., 2001]. Initial soil thickness was set to a uniform low value of 10 cm, representative of the thinner soils found on the most divergent parts of the landscape. Under the assumption that rivers remove any material that is delivered, soil was not allowed to accumulate in channel locations. Figure 2 shows the predicted soil depth values for CB-MR, illustrating the pattern of thicker soils in convergent topography (hollows), where most landslides are observed, and thinner soils on divergent slopes. While the general spatial pattern of soil depth in this landscape is well reproduced, this method does not account for local variability due to stochastic processes such as tree throw and animal burrowing that has been observed in this area [*Schmidt*, 1999; *Heimsath et al*., 2001].

Data on root cohesion as a function of depth at this site reported by *Montgomery et al*. [2009, Figure 7c], who measured the spatial distribution of root type, root diameter, root/area ratio, and root depth along the

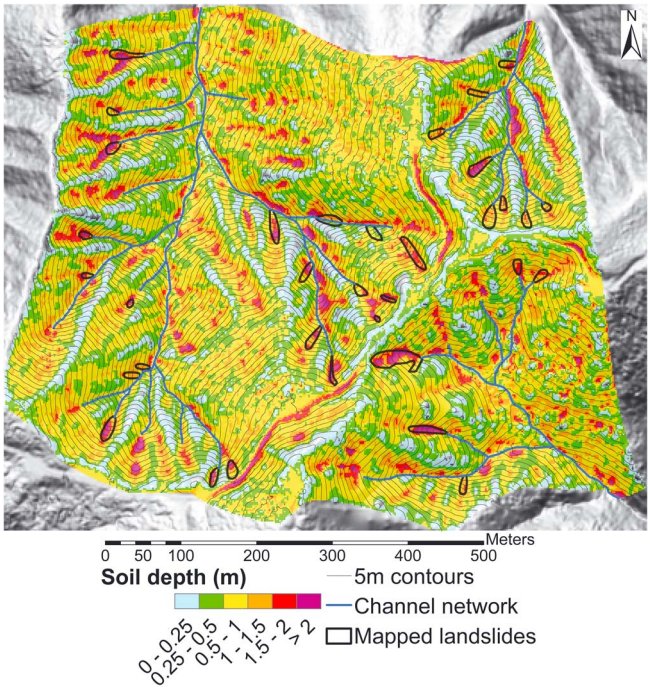

Figure 2. Predicted soil depth for CB-MR, resulting from the application of the coupled soil production and soil transport submodels (see text for parameters). Soils are generally thicker in the hollows, where most of the observed landslides (black outlines) are also located.

perimeter of the scarp of the CB-1 landslide, suggest that the relationship between root cohesion and depth at this site is better represented as an exponential function [e.g., *Dunne*, 1991; *Benda and Dunne*, 1997; *Roering*, 2008] of the form

$$C_b = C_{r0}e^{-zj} \tag{15}$$

where C_b (Pa) is the root cohesion at the base of a soil column of thickness z (m), C_{r0} (Pa) is the root cohesion value at the surface, and j (1/m) is the reciprocal of the e-folding depth of C_b (i.e., the depth at which C_b increases by a factor of e) [*Dunne*, 1991; *Benda and Dunne*, 1997]. The average lateral root cohesion C_l (Pa) per unit perimeter area is then the integral of C_b over the thickness of the soil z,

$$C_l = \frac{1}{z}\int_0^z C_{r0}e^{-z_c j}\mathrm{d}z_c = \frac{C_{r0}}{jz}\left(1 - e^{-zj}\right) \tag{16}$$

where z_c (m) is the vertical coordinate.

The coefficients C_{r0} and j are typically obtained either from field data or literature-based estimates of the relationship between root strength, root density, and depth. We extend the site-specific measurements reported by *Montgomery et al*. [2009] for the CB-1 landslide to the CB-MR study area, and set C_{r0} to 22 kPa and j to $5\,\mathrm{m}^{-1}$. The entire CB-MR area was clear cut in 1987 [*Torres et al*., 1998], and thus spatial variation in root strength may have been reduced. Although the model relating root cohesion and depth is spatially invariant (equation (15)), soil depth variability leads to variability in lateral and basal root cohesion (Figure 3), with observed landslides generally found in areas of low predicted root cohesion.

6.1.2. Hydrologic Conditions and Storm Sequence

The intensive field experiments at CB-1 demonstrated that nearly all storm runoff flows through a shallow fractured bedrock zone before exfiltrating back into the soil and flowing to the channel [e.g., *Montgomery et al*., 1997; *Torres et al*., 1998; *Montgomery and Dietrich*, 2002; *Montgomery et al*., 2009]. Patches of partial soil saturation resulting from this exfiltration developed along the topographic axis of the hollow [*Montgomery et al*., 2009, Figure 6]. The extensive studies performed at this site demonstrate that although highly variable, the patterns of elevated pore pressure are roughly consistent with a subsurface flow that follows a head gradient parallel to the topographic surface, a common assumption in shallow subsurface flow models

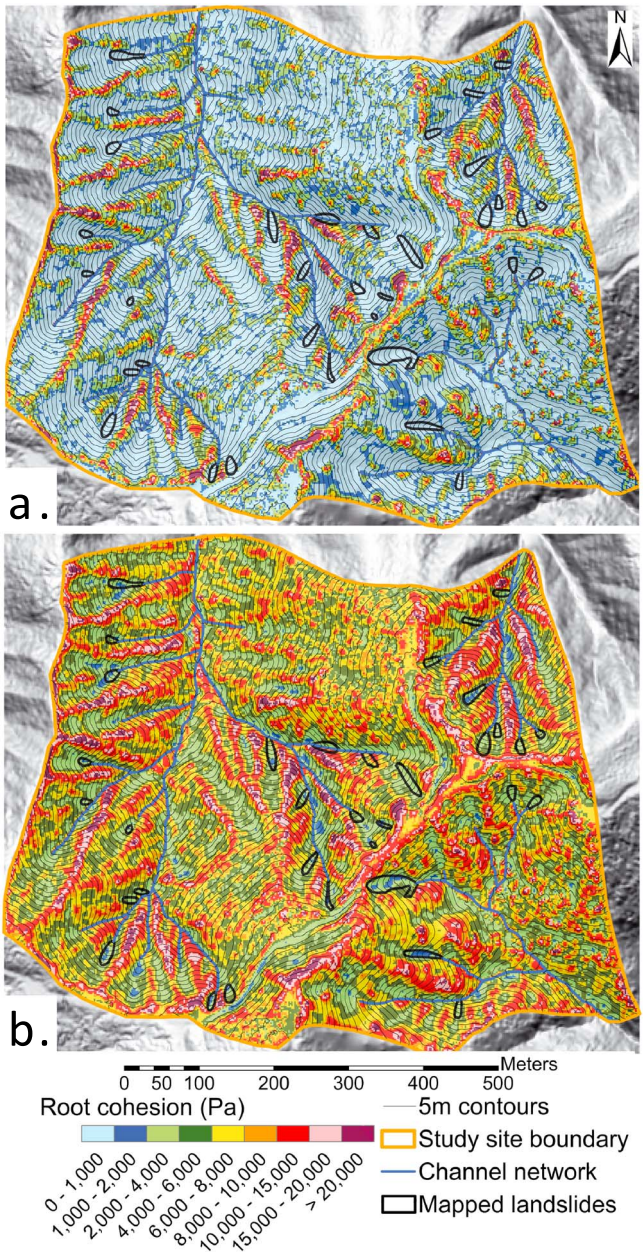

Figure 3. Predicted (a) basal and (b) lateral root cohesion for CB-MR, resulting from the application of equations (15) and (16) with CB-1 parameters (see text). The observed landslides (black outline) generally occur in areas of low predicted root cohesion.

[e.g., *Beven and Kirkby*, 1979]. As the spatial pattern of the conductive fractured bedrock zone is not known and extremely difficult to estimate, we make the assumption that storm runoff is confined to the soil layer and that the head gradient is equal to the topographic surface gradient, assumptions widely used by others [e.g., *Dietrich et al.*, 1992; *Montgomery and Dietrich*, 1994; *Wu and Sidle*, 1995; *Pack et al.*, 1998; *Montgomery et al.*, 2000; *Schmidt et al.*, 2001; *Borga et al.*, 2002; *Rosso et al.*, 2006; *Tarolli and Tarboton*, 2006]. We recognize that this is not an accurate representation of the complex hydrological processes which control storm runoff flow, but at this site these simplifications are useful to provide a good approximation to soil saturation patterns. The effect of these assumptions is generally to overestimate pore pressure in the soil but eliminate the local exfiltration-driven pore pressure spikes, which can localize landslides.

In order to model landslide response to specific storms, we use a form of the transient, topographically steered hydrologic model proposed and applied to the CB-MR site by *Rosso et al.* [2006]. While our landslide model is independent of the choice of hydrologic model, we choose this one as it is the simplest extension to steady state hydrologic models [e.g., *Beven and Kirkby*, 1979; O'Loughlin, 1986; *Moore et al.*, 1988; *Dietrich et al.*, 1992; *Montgomery and Dietrich*, 1994] and has been shown to capture the transient response at this site, thus allowing the application of storm time series. Pore pressure is modeled by coupling the conservation of mass of soil water with Darcy's law to describe seepage flow. This yields a simple analytical model capable of describing the combined effects of duration and intensity of a precipitation episode in triggering shallow landslides [*Rosso et al.*, 2006]. This model assumes that precipitation and transmissivity are spatially uniform and predicts for each grid cell the saturated height h_i (m) of the soil column z (m) at a discrete time step i as

$$h_i = q_i \frac{az}{Tb\sin\theta}\left(1-\exp\left(-\frac{1+v}{v-vS_r}\cdot\frac{Tb\sin\theta}{az}\right)t_i\right)+h_{i-1}\exp\left(-\frac{1+v}{v-vS_r}\cdot\frac{Tb\sin\theta}{az}\right)t_i \quad (17)$$

where q_i (m/d) is the effective precipitation at time step i, h_{i-1} (m) is the height of the saturated fraction at time step $i-1$, t_i (days) is the duration of time step i, v () and S_r () are, respectively, the void ratio (volume of voids divided by

Table 1. Storm Intensity/Duration Parameters Used for the Application of the Model to the CB-MR Study Site

Storm Year	1987	1990	1991	1992	1993	1996	1996 Detailed
Duration (days)	1	1	1	1	1	1	12.4 (10 min series)
Intensity (mm/h)	5.0	3.85	2.5	2.37	4.06	6.87	0.94 (peak hourly: 25.7)

the volume of solids) and degree of saturation (volume of water divided by the volume of voids) of soils, T (m^2/d) is the hydraulic transmissivity and the other parameters are defined as above. Under the assumption that hydraulic conductivity K (m/d) is uniform with depth [*Montgomery and Dietrich*, 1994], $T = Kz$, and equation (17) becomes

$$h_i = q_i \frac{a}{Kb\sin\theta}\left(1 - \exp\left(-\frac{1+v}{v - vS_r}\cdot\frac{Kb\sin\theta}{a}\right)t_i\right) + h_{i-1}\exp\left(-\frac{1+v}{v - vS_r}\cdot\frac{Kb\sin\theta}{a}\right)t_i \quad (18)$$

We use field-measured parameters obtained at CB-1, and set $v = 1$ [*Montgomery et al*., 1997], $S_r = 0.6$, equivalent to the 30% field capacity of soil in this location [*Torres et al*., 1998], and $K = 67$ m/d [*Ebel et al*., 2007b]. In this model, precipitation is instantaneously delivered to the saturated zone and head at each grid cell, h_i, instantaneously adjusts throughout the system.

The rain gauges at CB-1 provide a 10 min resolution time series of the November 1996 storm, the largest storm on record for the study area which triggered the CB-1 landslide and four others at CB-MR [*Montgomery et al*., 2009]. *Montgomery et al*. [2000] attributed the other (pre-1996) landslides at CB-MR to the most intense 24 h storms in the 6 years when landslides occurred. We use the characteristics of the six boxcar storms (storms of constant intensity for a specific duration, listed in Table 1) identified by *Montgomery et al*. [2000] to generate spatial layers of pore pressure using equation (18) and apply the model to each storm, generating independent landslide predictions. To avoid double counting, individual landslides are attributed to individual storms. All the landslides in the 10 year record failed at or very near the soil-bedrock interface [*Montgomery et al*., 2000], implying that locations where a landslide has occurred would not have enough soil to fail during a subsequent storm. Since modeled soil depth and topography do not vary dynamically through the storm sequence, we attribute landslides to individual storms, and in each subsequent simulation we retain only the landslides that do not overlap previous landslides, resulting in a final composite set of predicted landslides. We discuss possible impacts of the choice of this attribution method in section 7.1. To test the performance of the landslide model with a more complex rainfall time series (as opposed to constant-intensity boxcar storms), we also apply equation (18) to the 10 min resolution rainfall time series of the 1996 storm (referred to as "1996 storm", Table 1), up to the time of the CB-1 failure reported by *Montgomery et al*. [2009, their Figure 3]. This storm was the last and largest storm in the study period, thus in this test we ignore the previous storms and retain all the predicted landslides (i.e., assuming that failures that occurred in previous, smaller storms would also have occurred under the storm of record).

Figure 4 illustrates the spatial pattern of the soil saturation ratio (m) predicted by the hydrological model for the storms with lowest and highest 24 h intensities (2.37 and 6.87 mm/h), and the 1996 storm at the time of the CB-1 failure. Water table heights are always higher in the hollows than on divergent slopes, but areas with deepest soils where some of the observed landslides are only moderately saturated, while moderately divergent areas where soils are thin can be more saturated, suggesting that saturation alone is not the primary control on instability. The extent of saturated areas increases significantly with increasing precipitation intensity. The boxcar and the detailed representation of the 1996 storm result in similar pore water pressure fields (Figures 5b and 5c) with average difference $<15\%$.

6.2. Comparison of Observed and Predicted Landslides

6.2.1. General Characteristics

Landslides in both predicted and observed groups have sizes ranging from a few square meters to hundreds of square meters, are generally longer than they are wide, and are principally located in topographic hollows where soil and water tend to accumulate (Figure 5). Predicted landslides rarely extend out of the parts of the hollows with the thickest soils, consistent with the 10 year observational record. The mean size of the predicted landslides is 200 m^2 and 197 m^2, with standard deviation (STD) of 193 m^2 and 201 m^2, for the composite and 1996 storm cases, respectively. This is ~0.85 times the mean observed size (234 m^2, 191 m^2 STD). The mean failure depth for predicted landslides 1.43 m and 1.33 m, with STD of 0.7 m and 0.6 m, for the composite and 1996

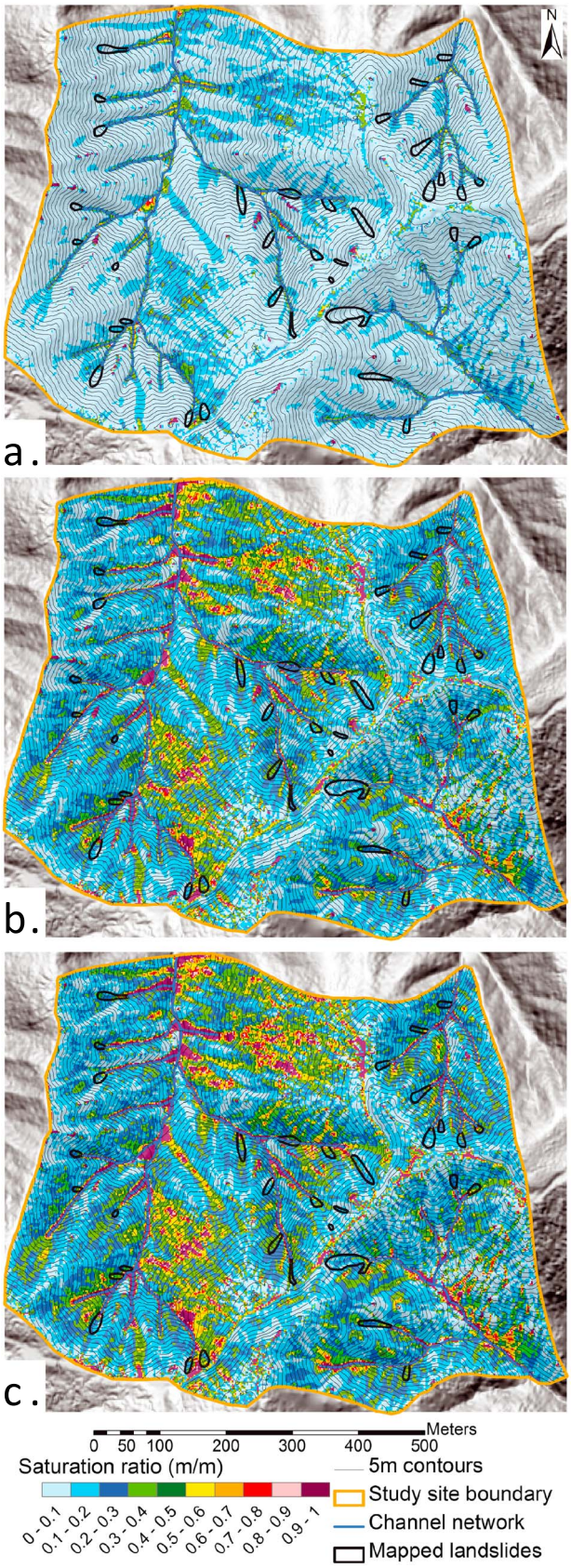
N
a.
b.
c.
Meters
0 50 100 200 300 400 500
Saturation ratio (m/m)
0 - 0.1
0.1 - 0.2
0.2 - 0.3
0.3 - 0.4
0.4 - 0.5
0.5 - 0.6
0.6 - 0.7
0.7 - 0.8
0.8 - 0.9
0.9 - 1
5m contours
Study site boundary
Channel network
Mapped landslides

Figure 4

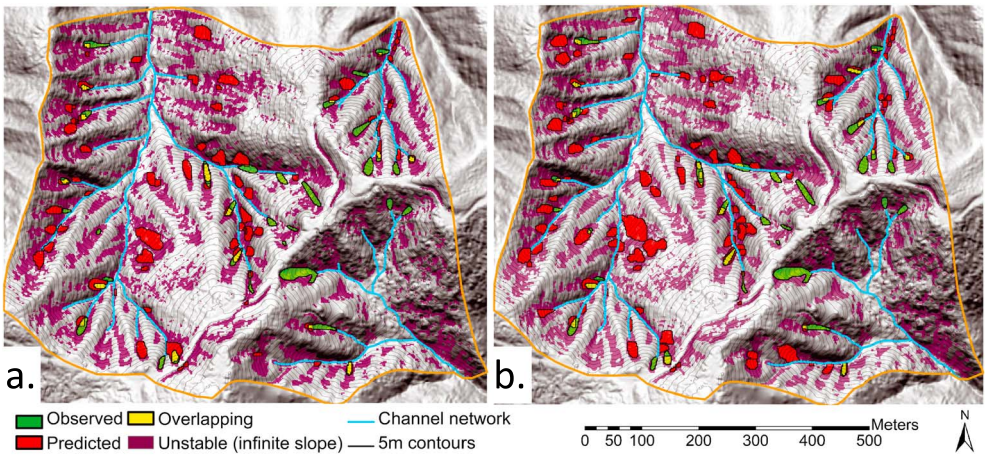

Figure 5. Results of the application of the model to the CB-MR study area using the base case parameterization ($\phi = 40°$, $C_{r0} = 22$ kPa) showing (a) the composite map of discrete landslides predicted for the storm sequence identified by *Montgomery et al.* [2000] (see text for details) and (b) the map of landslides predicted using the 1996 storm time series. Predicted landslides are shown in red, and observed landslides are shown in green. Grid cells which are in both the predicted and observed sets are shown in yellow. Grid cells which are unstable according to the identically parameterized infinite-slope model are shown in purple.

storms, respectively, while the predicted mean soil depth for the observed landslides is 1.41 m (0.4 m STD). These are very similar to the mean depth of 1.38 m from the subset of observed landslides that were field mapped [*Montgomery*, 1991; *Larsen et al.*, 2010], suggesting that our soil depth model broadly captures the observed spatial variations in soil thickness. The majority of the observed landslides (56% and 65% for the composite and 1996 storm cases, respectively) overlap with predicted landslides, but there are more than twice as many landslides predicted as observed in both the composite (89) and 1996 storm (130) cases.

Following *Dietrich et al.* [2001], we compute the percentage of observed landslides captured by our simulations and the percentage of the landscape covered by predicted landslides. The model captures 56% of the observed landslides using the FS_{min} pruning method with the composite storms and 65% with the 1996 storm and predicts that landslides cover 3.5% and 5.5% of the landscape, respectively (Figure 6), compared to 1.8% in reality. Similar results (not shown) are obtained using FS_{max} pruning, with one more landslide captured in the 1996 storm case (68% of total, with predicted landslides covering a further 0.8% of the landscape). Despite the modest overprediction, the percentage of correctly predicted stable area is considerable (97% and 95% in the FS_{min} composite and 1996 storm cases, 97% and 94% in the FS_{max} composite and 1996 storm cases, respectively).

Landslide sediment volume for the 10 years after forest clearing is calculated by summing the predicted soil depths for all grid cells that fall within landslides. The total landslide volume for the observed failures is 11,400 m^3. This volume differs from the 8700 m^3 reported by *Montgomery et al.* [2000]; this difference may in part be due to the use of constant (rather than modeled) soil depth in *Montgomery et al.* [2000]. The predicted volume from the composite application is approximately twice that observed (22,800 m^3); this overprediction is expected since we neglect the legacy of landslides prior to the first storm in the series but suggest that the predicted sediment volume is of the right order of magnitude.

6.2.2. Temporal Sequence

Approximately half of the predicted landslides occur in the first storm (the second largest in the sequence), which is consistent with the observations of *Montgomery et al.* [2000] (Figure 7). However, a similar number occurs in the last storm (the largest of record), which is inconsistent with the observations (Figure 7). The FS_{max} pruning method produces similar results. *Montgomery et al.* [2000] attribute the limited number of

Figure 4. Predicted spatial pattern of the soil saturation ratio, *m*, for boxcar representations of the 24 h storms with (a) lowest and (b) highest intensities (2.37 and 6.87 mm/h, respectively); and (c) the pattern of *h* resulting from the 10 min time series of the 1996 storm at the time of the CB-1 failure. *h* is less than or equal to the soil depth *z* and is higher in convergent topography (hollows) as well as in mildly convergent, high-drainage area locations, where water table heights increase with precipitation intensity.

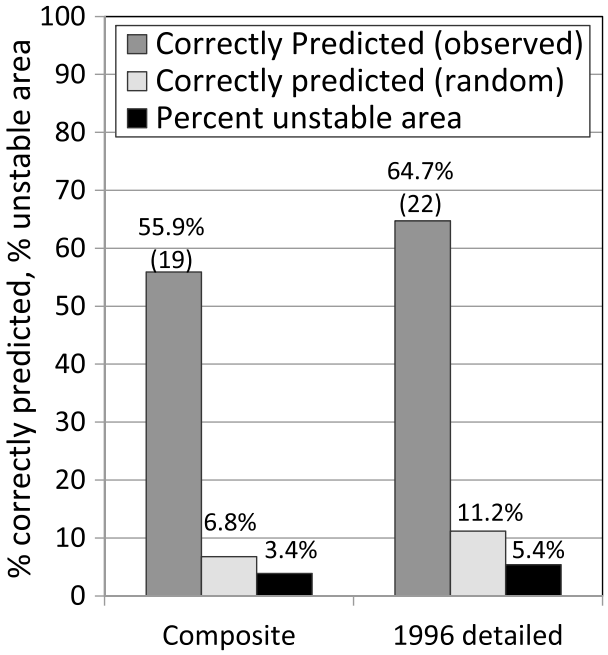

Figure 6. Performance of the model using the base case parameterization ($\phi = 40°$, $C_{r0} = 22$ kPa) and the FS_{min} pruning method for the storm parameters described in Table 1. The dark gray bars show the percentage of the 34 observed landslides (with the absolute number in parentheses) captured (i.e., overlapped by a prediction) by the composite predictions resulting (left) from the six 24 h storms, and (right) from the application of the 10 min time series of the 1996 storm. The light gray bars show the percentage of landslides that would be captured were they be randomly distributed. The black bars show the cumulative percentage of the landscape area classified as unstable.

landslides in the 1996 storm (<15% of the total) to the prior failure of the most susceptible areas and to the regeneration of root strength 9 years after cutting. These effects are not captured in our simulations, which do not consider landslides prior to the first storm (our soil depth model implicitly assumes that hollows were continuously filling with soil for 6000 years, see section 6.1.1) and use time invariant root strength parameters. *Montgomery et al*. [2000] also report that the lower intensity storms (storms 2–5) contributed a significant number of landslides to the total. In our simulations these storms individually have the potential to cause many landslides (Figure 7), but as these overlap with landslides from the first storm, they are not retained. In the field case, sites that remained stable in the first storm then subsequently fail in a lower intensity storm suggest that landslide-relevant hillslope characteristics (e.g., soil strength, root cohesion, and preferential flow paths) other than rainfall vary on annual to decadal timescales.

6.2.3. Frequency Distributions of Size and Location

We compare the probability density functions (PDF) of planimetric area and median topographic index for observed and predicted landslides (see section 2.3). The topographic index I_T (m) is defined as follows [*Dietrich et al*., 1992]:

$$I_T = \log\left(\frac{A}{b\sin(\theta)}\right) \tag{19}$$

where A is the drainage area (m^2), b is the grid cell size (m), and θ is the slope angle. Low index values are in steep, nonconvergent areas, whereas high index values are farther down the valley axis where drainage area is larger and slope is gentler.

The nonparametric two-sample Kolmogorov-Smirnov (K-S) test is used to evaluate the probability of obtaining the predicted and observed CDFs from the same underlying distribution [*Conover*, 1971]. Because this test is solely based on the maximum vertical distance between the CDFs, it is a rather strict test. Other nonparametric statistics, such as the Cramer-Von Mises and the Mann-Whitney tests, differ from the K-S test by adopting more specific definitions of distance but are similarly strict. Perhaps for this reason, none of the attempts to predict or characterize landslide size distributions report the results of a nonparametric statistical similarity test of modeled and observed distributions. The null hypothesis in the K-S test is that the CDFs originate from the same distribution. Low probabilities (p values) imply that the null hypothesis can be rejected [*Dallal*, 2012]. In our case good model performance would result in acceptance of the null hypothesis that modeled and observed size and location distributions originate from the same underlying distribution, with larger p values indicating better model performance.

Predicted landslide size distributions have a modes similar to the observed distribution but with heavier tails, oversampling small and large landslides relative to the observations, and a stronger bias toward smaller landslides (Figure 8a). Maximum, mean, median, and standard deviation of sizes of predicted landslides are within a factor of 1.5 of the observed values (Table 2). Our model underestimates minimum size, predicting

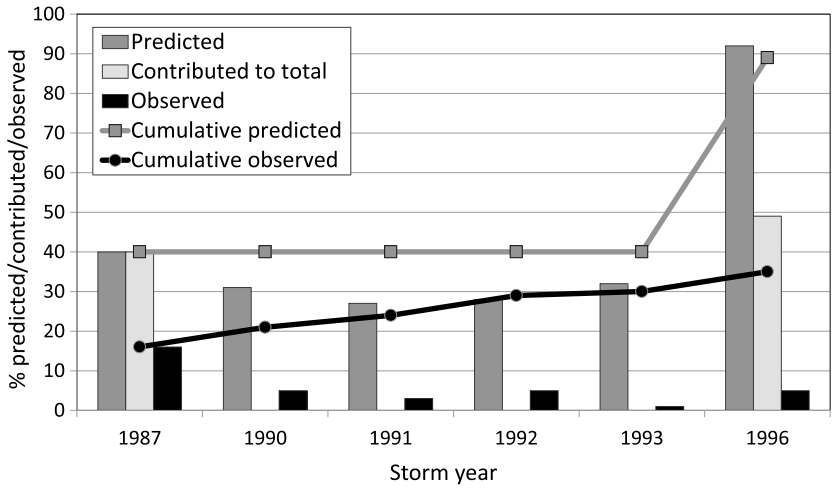

Figure 7. Results of the composite six-storm application of the model to the CB-MR study area showing a bar graph of the number of landslides predicted using the base case parameterization ($\phi = 40°$, $C_{r0} = 22$ kPa) in each of the six 24 h storm simulations, the number of new landslides added by each simulation to the composite results, and the corresponding observations listed by *Montgomery et al.* [2000], using the FS_{min} pruning method; lines show the cumulative number of predicted and observed landslides for the storm sequence.

failures of a few single cells, while the minimum observed landslide is comprised of nine cells (Table 2). Neither the storm type (composite or 1996 storms) nor the type of pruning (FS_{min} or FS_{max}) noticeably alters the size distributions (Table 2). However, all modeled size distributions are significantly different from the observed (i.e., null hypothesis is rejected) at the 95% confidence level according to the K-S test (Table 2). In each case this is the result of overprediction of small landslides (Figure 8a), and by censoring landslides smaller than the smallest observed, the null hypothesis can no longer be rejected at the 95% confidence level, though differences remain significant at confidence levels between 67% and 84% (Table 2).

The modeled I_T distribution closely matches the range and the mode of the observations (Figure 8b), reflecting locations mostly predicted along the hollow axis (Figure 5). Predicted PDFs are marginally broader than the observed PDF, with the predictions exhibiting a slight bias toward lower topographic indices. Minimum, maximum, mean, and median of I_T of predicted landslides are within factors of 3, 2, 2.5, and 1.5 of the observed, respectively (Table 2). While modeled standard deviation differs from the observed by less than a factor of 2 for the composite simulation, it differs up to a factor of 8 for the 1996 storm simulation.

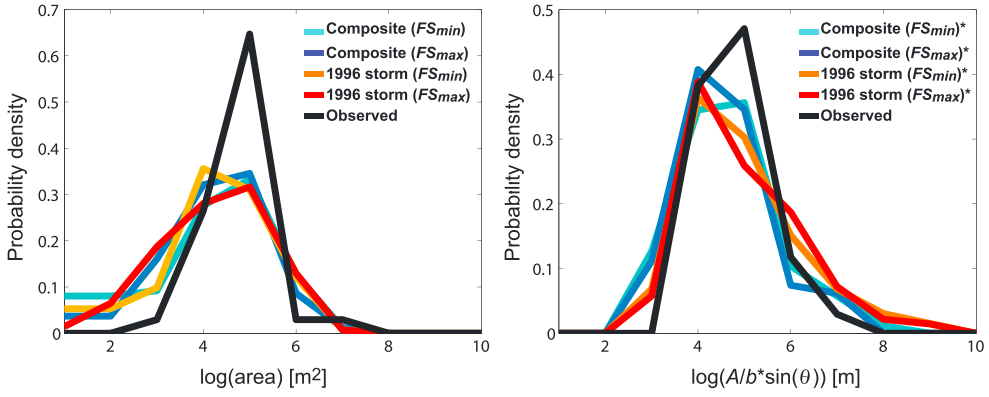

Figure 8. Probability density functions of (a) size and (b) topographic index of landslides in the CB-MR study area. Black lines represent the observed landslides. Colored lines represent the composite predictions using the base case parameterization ($\phi = 40°$, $C_{r0} = 22$ kPa) resulting from the chronological application of six individual 24 h duration storms with varying intensity (cool colors) and from the application of the 1996 storm time series (warm colors). Antecedent moisture conditions are set to 30%. Aserisks in the legend denote the distributions that are not significantly different from the observed distributions at a 95% confidence level using a two-sample K-S test. Note different vertical scales in Figures 8a and 8b.

Table 2. *P* Values, and Summary Statistics for Predicted and Observed Size and Location Distributions[a]

	Size (Planimetric Area (m^2))						Location (Median Topographic Index I_T (m))					
Distribution	*p* Value	Min	Max	Mean	Median	STD	*p* Value	Min	Max	Mean	Median	STD
Observed		36	1132	233	182	191		70	1554	274	213	268
Composite FS_{min}	0.001	4	1176	184	132	192	0.331	28	3096	326	159	491
Composite FS_{max}	0.014	4	1372	188	140	214	0.136	24	2677	279	137	422
1996 storm FS_{min}	0.01	4	1500	187	128	200	0.297	25	1598	648	192	1706
1996 storm FS_{max}	0.003	4	1252	207	116	234	0.165	30	1962	698	178	2211
Composite FS_{min} ($\geq$36 m^2)	0.332	36	1176	221	166	192	0.617	28	3095	358	174	529
Composite FS_{max} ($\geq$36 m^2)	0.177	36	1372	213	156	218	0.319	24	2677	303	152	444
1996 storm FS_{min} ($\geq$36 m^2)	0.167	36	1500	212	152	203	0.281	25	1598	707	195	1819
1996 storm FS_{max} ($\geq$36 m^2)	0.164	36	1252	248	164	241	0.225	32	1962	556	195	1590

[a]Composite refers to the six-storm composite simulation, and 1996 storm refers to the single application of the 10 min 1996 storm time series, both using the base case parameterization. FS_{min} and FS_{max} indicate the pruning method used. Rows labeled with $\geq$36 m^2 refer to the same simulations but without landslides $<$36 m^2 (the smallest observed size).

The *p* values in the K-S test are considerably higher for the I_T distributions, suggesting that location is captured more accurately than size. While in the case of location the null hypothesis cannot be rejected with 95% confidence, differences remain significant at confidence levels between 67% and 86% (Table 2). Censoring small landslides only moderately increases the *p* values, suggesting that in this case errors are not solely due to the overprediction of small landslides.

We test the ability of our model to capture both location and size by comparing the size of predicted and observed landslides in cases where they overlap. For this subset of the data, there is only moderate agreement: 13% of predicted landslides have size that is within a factor of 1.25 of the observed; 28% have size within a factor of 1.5 of the observed; 45% have size within a factor of 1.75 of the observed; and 55% have size within a factor of 2 of the observed (Figure 9). Predicted size spans almost twice the range of observed size. In the composite case, predicted landslides range from 64 to 724 m^2 (mean = 282 m^2), while the corresponding observed landslides range from 88 to 380 m^2 (mean = 215 m^2). In the 1996 storm case, predicted landslides range from 44 to 660 m^2 (mean = 247 m^2), while the corresponding observed landslides range from 60 to 380 m^2 (mean = 212 m^2). The average ratio of predicted to observed size for individual landslide pairs is 1.4 and 1.6 for the composite and 1996 case, respectively, a significant increase from the general predicted to observed size ratio of 1.0 and 1.1 for the two cases, respectively.

Table 2 suggests that the choice of pruning method used in these simulations does not significantly impact the overall comparison of predicted and observed landslide characteristics. However, Figure 10 shows slight differences in the size and location of predicted landslides using the two methods. In particular, two landslides in the middle hollow predicted using FS_{min} pruning (labeled D and E in Figure 10a) are replaced by a single larger landslide when FS_{max} pruning is applied (labeled DE in Figure 10b). This suggests that the overall pattern of landslide occurrence may be captured using either pruning method, but the form and location of failure at a specific site may differ. This effect is small relative to the uncertainty in spatially varying parameters such as pore pressure and root cohesion (section 6.2.6).

6.2.4. Comparison With a Random Model

We test the null hypothesis that landslides are captured by the model due to chance alone by measuring whether the model captures more observed landslides than randomly distributed landslides. This is done by taking the average performance for 10 sets of randomly placed elliptical landslides with the same spatial density and size as the observed landslides but locations (*x*-*y* coordinates) and orientations (angle of major axis from north) selected using a random number generator (with ellipses not allowed to overlap) [*Spowart et al.*, 2001]. The results indicate that the null hypothesis can be rejected: in every case, the model captures 6–8 times as many observed landslides as random landslides (Figure 6), with the pruning method making little difference (not shown).

6.2.5. Comparison With Infinite-Slope Model

Our approach is compared with the commonly used infinite-slope approach (e.g., review in *Sidle and Ochiai* [2006]) using exactly the same parameters in both cases. The infinite-slope factor of safety FS_{inf} () is calculated from

$$FS_{inf} = \frac{C_b + (\gamma_s z - \gamma_w h)\cos^2\theta \tan\phi}{z\gamma_s \cos\theta \sin\theta} \quad (20)$$

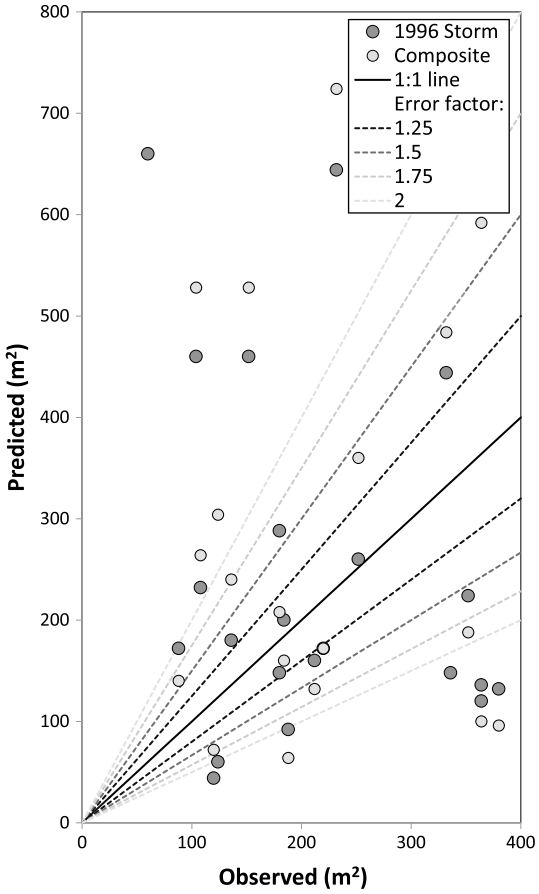

Figure 9. Comparison of predicted and of observed sizes for overlapping landslide pairs for the application of the detailed 1996 storm time series and the composite six-storm sequence. Solid line is the 1:1 line, while dashed lines indicate error factors of 1.25 to 2 (e.g., for an error factor of 2 predicted size is between half the size and twice the size of that observed). The average predicted to observed size ratio is 1.6 (1996) and 1.4 (composite) for individual landslide pairs, compared to the overall average of 1.1 (1996) and 1.0 (composite), with the size of predictions spanning almost twice the range of the observations.

The infinite-slope method captures 100% of the observed landslides, suggesting that it may be effective at the simpler task of delineating areas of landslide susceptibility (Figure 5). However, in contrast to our model, it does not delineate individual landslides (and thus their size) and it considerably overpredicts the unstable area (composite = 28%; 1996 storm = 31%) compared to our approach (3.4% and 5.4%). Not surprisingly, this overprediction results in a reduction of the percent of the stable area correctly predicted (73% and 70%), compared to our model (97% and 95%).

6.2.6. Success Rate and Sensitivity to Parameter Variations

To explore our approach's sensitivity to parameter variation, success rate curves (see section 2.3) are constructed by varying parameters one at a time from the base case parameterization: soil friction angle $\phi = 40°$, storm intensity $q_i = 10$ min precipitation time series from CB-1 rain gauge (maximum intensity of 42 mm/h), and surface root strength $C_{r0} = 22$ kPa. The parameter ranges are based on their estimated variability at this site: ϕ is varied from 35° to 45° [*Montgomery and Dietrich*, 1994], C_{r0} is rescaled from 0% to 200% (0–43 kPa) [*Schmidt et al*., 2001], and q_i from 0% to 200% (maximum intensity of 85 mm/h) [*Montgomery et al*., 2009]. This produces a set of success rate curves expressing landslide capture rate as a function of total predicted unstable area. Best performance is achieved when landslide capture rate is maximized and total predicted unstable area minimized; i.e., the curve is closer to the top left corner of the plot.

Figure 11a shows that the percent of landslides captured by our model (SA curves in Figure 11a) as a function of the percent of the landscape classified as unstable is extremely sensitive to this parameter variation. For example, rescaling the storm intensity results in 0% to 97% of landslides being captured (Figure 11a). Varying friction angle or root cohesion parameters produces almost identical results, with the success rates following similar curves. In contrast to the extreme variation in the percent of observed landslides overlapped by predictions, the change in percent of landscape predicted as unstable is relatively modest, ranging from 0% to 14% (Figure 11a). Perfect recall (100% landslides captured) within this parameter range is achieved by our model only by varying a combination of the parameters (the four filled yellow circles in Figure 11a), with the best case involving halving C_{r0} (11 kPa), with $\phi = 35°$ and the base case rainfall resulting in less than 13% of the landscape unstable. The insets in Figure 11 show a ratio of benefit, the percent of landslides correctly predicted (PLC), to cost percent landscape predicted as unstable (PUL), as the three parameters are varied. Under the assumption that PUL and PLC are equally weighted, higher values of this ratio indicate improved model performance. The PLC/PUL ratio increases with increasing friction angle

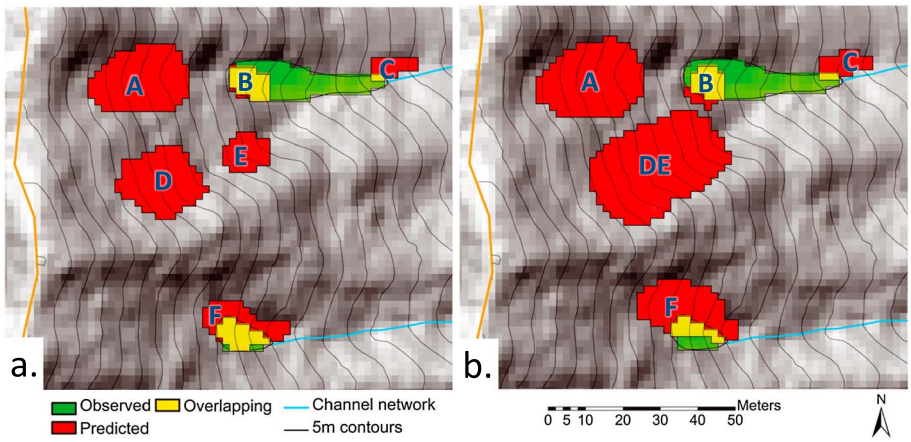

Figure 10. Detail from the northwestern section of the CB-MR study area comparing the two different methods for pruning overlapping landslide predictions: (a) predictions resulting from retaining the unstable shapes with FS_{min} and (b) predictions resulting from retaining the unstable shapes with FS_{max}, both obtained using the base case parameterization ($\phi = 40°$, $C_{r0} = 22$ kPa). Predicted landslides are shown in red, and observed landslides are shown in green. Grid cells that are in both the predicted and observed sets are shown in yellow. The two methods result in landslides with slightly different locations and sizes. In particular, predictions D and E in Figure 10a are combined into a single landslide DE in Figure 10b. The 1996 storm 10 min time series was used in both panels.

(Figure 11b) and root cohesion (Figure 11c) and decreases with increasing storm intensity (Figure 11d). It is important to note that in practice cost/benefit weights depend on the specific application. For example, in forest management it may be more important to efficiently reduce the areas where logging may occur than to predict all landslides (i.e., favoring reduced cost). In contrast, if human lives are at stake it may be more important to predict all possible landslides than to minimize the percent of the landscape predicted to be unstable (i.e., favoring increased benefit). Nevertheless, the PLC/PUL measure can be a useful tool to calibrate the model parameterization to the goals of a specific application.

Very different success rate curves are obtained when applying these parameterizations to the infinite-slope model (IS curves in Figure 11a). For the base case parameters ($\phi = 40°$, $q_i = 10$ min time series, $C_{r0} = 22$ kPa), and for all other parameter values described above, all observed landslides are overlapped by predictions (100% captured). Parameter variation instead greatly changes the percent of the landscape estimated to be unstable (the set of open symbols in Figure 11a). The choice of which parameter to vary makes a bigger difference in this case, with storm intensity resulting in 14–43% PUL and root strength in 25%–67% PUL, with friction angle taking intermediate values (Figure 11a). Within this parameter set, the best performance was obtained with no rainfall, with $<$14% unstable landscape (the top leftmost blue diamond in Figure 11a). The lower left end of the IS curves overlaps with the upper right end of the SA curves. This overlap occurs only when the two methods are at opposite extremes in their parameter sets ("weak", i.e., low friction angle, low cohesion, high storm intensity, for the SA case; "strong", i.e., high friction angle, high cohesion, low storm intensity for the IS case). Under these "effective" parameterizations, the performance of the two methods is very similar. However, the PLC/PUL curves for our model are consistently higher than those for the infinite-slope model (Figures 11b–11d), with the exception of the case of no precipitation where none of the observed landslides are predicted to fail by our model resulting in a PLC/PUL value of zero in spite of the minimal fraction of landscape predicted to be unstable (0.2%). In contrast, the infinite-slope model predicts observed failures even in the absence of precipitation, resulting in a positive PLC/PUL value in spite of 14% of the landscape predicted to be unstable (Figure 11d).

6.2.7. Independent Test of Slope Stability Model

The majority of observed landslides are overlapped by a predicted landslide using our base case parameters ($\phi = 40°$, $q_i = 10$ min time series, $C_{r0} = 22$ kPa), but the predicted landslide scars often only partially coincide with the observed scar outline. As a separate test, the MD-STAB slope stability model is applied to the specific locations and observed dimensions of the 34 landslides identified by *Montgomery et al.* [2000] using the same parameterization. For this site-specific application only 6% of the observed landslides are predicted to be unstable for the composite storm case and 12% for the detailed 1996 storm case. This low frequency of

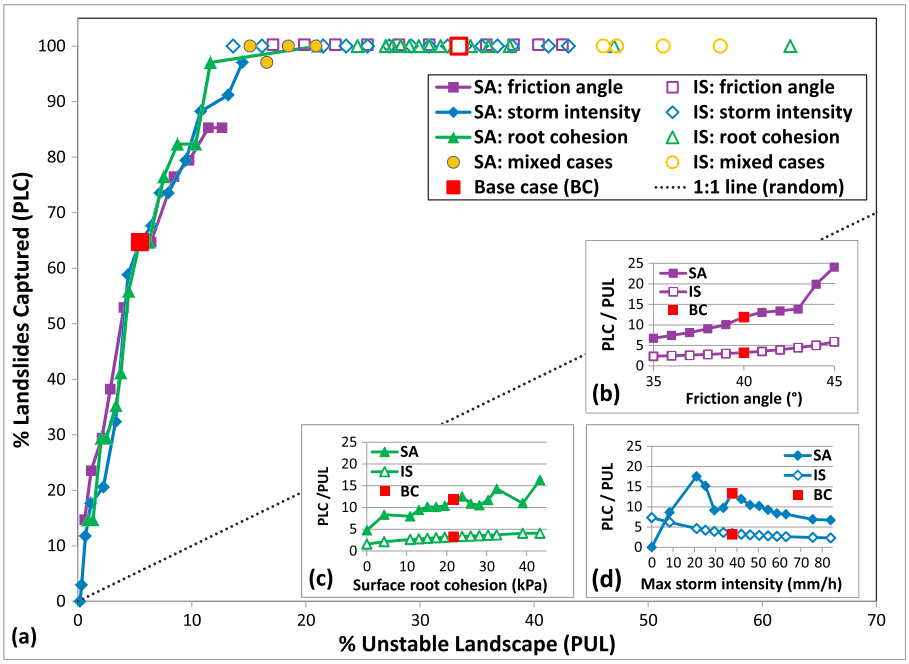

Figure 11. (a) Comparison of success rate curves from the application of our model (SA) and of the identically parameterized infinite-slope model (IS). Each curve results from individually varying friction angle, storm intensity, and root cohesion parameters (see text). The two individual red squares show the performance of the two models with the base case parameterization for the 1996 storm ($\phi = 40°$, $q_i = 10$ min time series, $C_{r0} = 22$ kPa). Insets show the benefit/cost ratio, defined as the % landslides captured (PLC)/% unstable landscape (PUL), for the two models as (b) friction angle, (c) maximum root cohesion, and (d) maximum storm intensity parameters are individually varied, with the base case scenario indicated by red squares in the insets.

predicted instability suggests that the factor of safety of the observed landslides is overestimated by MD-STAB. Applying the parameter range defined in the previous section (Figure 11), we find that the number of observed landslides classified as unstable using MD-STAB increases when the friction angle is decreased (up to 56% predicted unstable for $\phi = 35$), when the rainfall intensity time series is increased (up to 50% for double intensity), and when the maximum surface root cohesion is decreased (up to 82% for no cohesion). MD-STAB's inability to capture all observed landslides could be attributed to model error, model parameterization, and/or mapping errors, discussed in section 7.1.

6.2.8. Independent Test of Search Algorithm

Many factors contribute to the ultimate outcome of our model, from the correctness of the slope stability model, its submodels and their parameterization, to the accuracy of topographic data and of the validation data sets (see section 7.1). Nevertheless, because the search algorithm is general (i.e., it is compatible with a vast range of submodels and parameterizations), it is useful to evaluate its effectiveness given a specific model choice and parameterization (i.e., evaluating the error in the search algorithm, all else being equal). A definitive evaluation method would require knowing all the possible unstable landslides for a given set of model choices and parameterizations and checking how many of them are found by the search algorithm. Because the list of all possible landslides is unknowable (it would require an exhaustive exploration of all the possible configurations of grid cells), we use a much less stringent criterion: for the wide parameter exploration described in section 6.2.6 we test that any time an observed landslide shape is classified as unstable (i.e., FS < 1, as computed by MD-STAB), it is overlapped by an unstable prediction of the search algorithm. This test is embedded in the search algorithm computer code and is automatically executed every time the algorithm is presented with a set of observed landslides, logging an error message in case of no overlap with a prediction. We find that in every case where an observed shape has a calculated FS < 1 the search algorithm predicted at least one landslide that overlapped the observed shape. This suggests that missed landslides (i.e., false negatives) in the CB-MR application are the result of errors in the structure of the slope stability model or in its parameters rather than in the search algorithm.

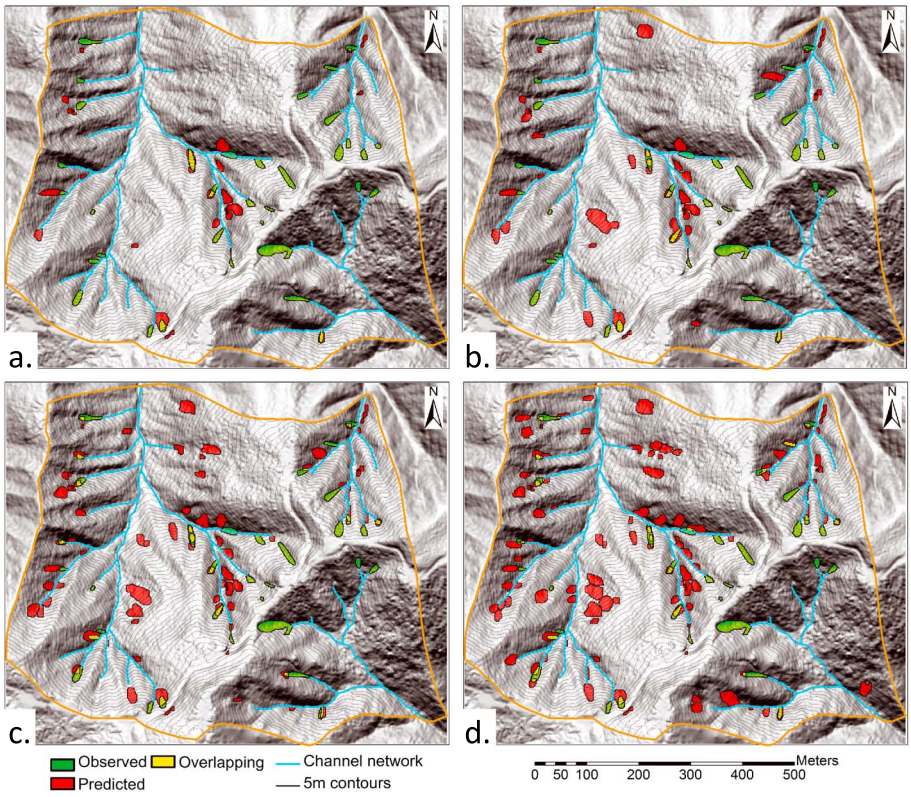

Figure 12. Predicted landslides resulting from application of the model to the CB-MR study area for boxcar storms of increasing intensity and with other values from the base case parameterization ($\phi = 40°$, $C_{r0} = 22$ kPa). Predicted landslides are shown in red, and observed landslides are shown in green. Grid cells which are in both the predicted and observed sets are shown in yellow. Rainfall intensities used are 2.37 mm/h (not shown), 3.49 mm/h (not shown), (a) 4.62 mm/h, (b) 5.74 mm/h, (c) 6.87 mm/h, and (d) 8.0 mm/h.

6.3. Impacts of Rainfall Intensity and Root Cohesion on Landslide Location and Size

Our approach is applied to CB-MR under varying rainfall intensity and root cohesion over a range representative of Oregon Coast Range conditions to explore impacts on landslide abundance, location, and size. Six 24 h boxcar rainfall intensities are chosen by linearly interpolating between the lowest and highest intensity storms of the sequence identified by *Montgomery et al.* [2000] (with return periods of ~1 and ~70 years), and a higher intensity storm is added by extrapolating the intensity-duration-frequency curve computed by *Montgomery et al.* [2000] for the study area to ~100 year return level. The resulting intensities vary from 2.4 to 8 mm/h. To vary root cohesion we linearly interpolate between the clear-cut and natural forest values reported by *Schmidt et al.* [2001]. The resulting C_{r0} values range from 14 to 51 kPa, which at CB-1 would correspond to average lateral root cohesion (C_l) values ranging from 3 to 11 kPa. In this application we use the highest intensity boxcar storm (8 mm/h) to ensure that landslides are predicted under very high root cohesion.

Figures 12 and 13 show landslides predicted under increasing storm intensity and decreasing root cohesion. As intensity increases or root cohesion decreases, the number of landslides increases, progressively affecting new areas in the landscape. Nevertheless, landslides continue to be predicted in steep, convergent areas, and their size remains broadly consistent with observed landslides.

Figure 14 shows the size and location distributions from these simulations. With increasing rainfall intensity the size distribution shifts to the right, reflecting an increase in the average landslide size (Figure 14a). Increasing rainfall intensity also causes landslides to shift down the hollow axis to locations with larger topographic index (Figure 14b). With increasing root cohesion the size distribution also shifts toward larger landslides (Figure 14c), but the distribution of locations generally becomes narrower, with little change in its mode (Figure 14d).

Changes in locations of landslides under these simulations are also reflected in the slope-area plots shown in Figure 15. Under low rainfall intensity, landslides only occur in areas of steep slopes and expand to areas of

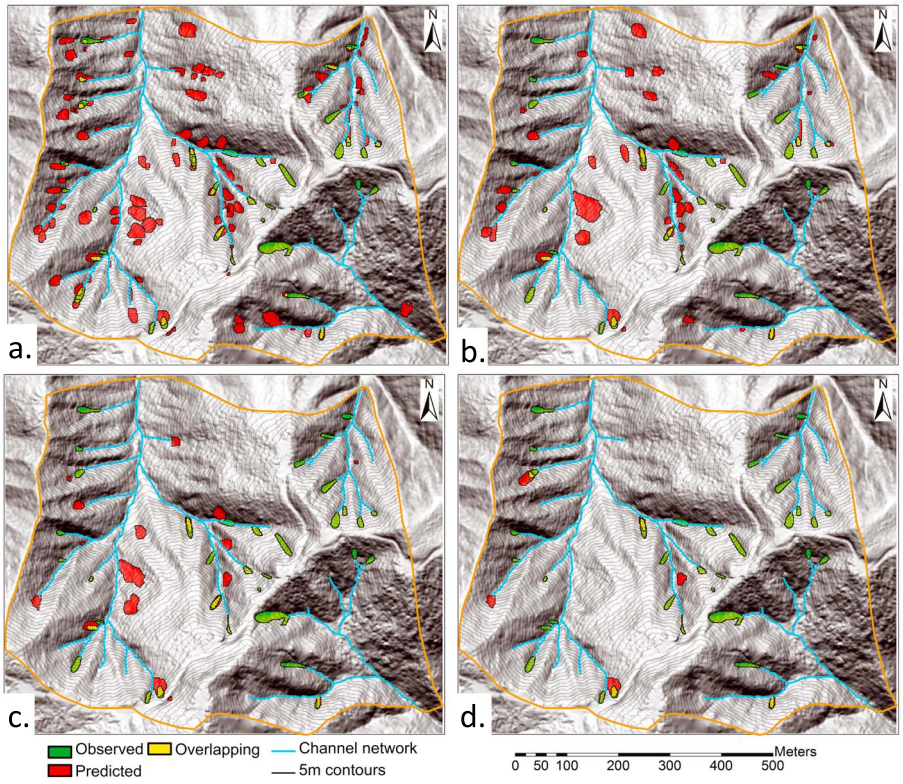

Figure 13. Predicted landslides resulting from application of the model to the CB-MR study area for the high-intensity (8 mm/h) boxcar storm under increasing root strength and with friction angle from the base case parameterization ($\phi = 40°$). Predicted landslides are shown in red, and observed landslides are shown in green. Grid cells which are in both the predicted and observed sets are shown in yellow. C_{r0} values used are 14 kPa (not shown), (a) 22 kPa, (b) 29 kPa, (c) 37 kPa, (d) 44 kPa, and 51 kPa (not shown).

lower slope (but with higher drainage area for any given slope) with increasing rainfall intensity (Figure 15a). Similarly, landslides extend to a wide range of slopes and locations with larger drainage area under low root strength but become increasingly clustered toward the intermediate part of this range under increasing root cohesion (Figure 15b).

7. Discussion

7.1. Sources of Error in Predicting Landslide Size and Location

At CB-1, where local conditions were well constrained, the model predicts a landslide overlapping the observed landslide and within 13% of its size [*Bellugi et al.*, 2015]. At CB-MR, where local conditions are less well constrained, more than 35% of landslides are not predicted (Figure 5) and, of those that are, less than 55% have sizes within a factor of 2 of that observed (Figure 9).

More of the observed landslides can be captured under alternative parameter sets (Figure 11a) but with an associated increase in the predicted unstable fraction of the landscape. Rather than tuning the model to optimize performance at this location we aim to understand why the base case parameter set (i.e., the best independent estimate of parameters) fails to fully capture the observed landslides.

Assuming that observed landslides are correctly mapped, this failure could result from errors in the slope stability model, the search algorithm, or the parameters used. We have shown that the error is unlikely to be due to the search algorithm, since whenever MD-STAB predicts that an observed landslide is unstable, the search finds an overlapping landslide (section 6.2.8).

Parameterizing our model at the landscape scale, even for an area as small as CB-MR, is extremely difficult. Cyclical soil infilling by biogenic transport and evacuation by landslides [*Dietrich and Dunne*, 1978; *Lehre*, 1981; *Reneau and Dietrich*, 1987a] leads to a strong dependence of soil depth, and thus stability, on a

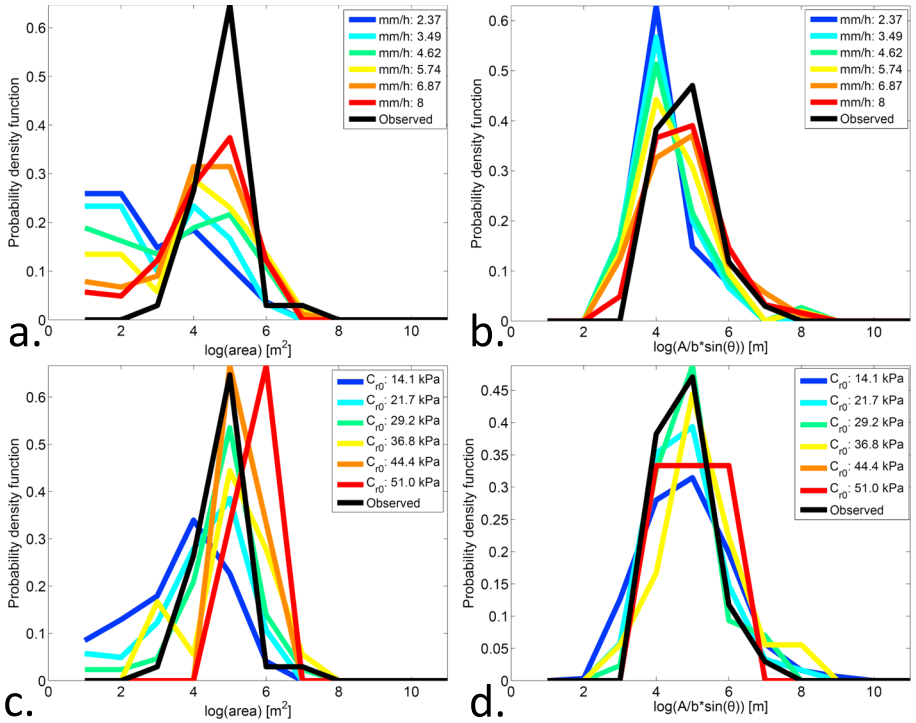

Figure 14. Probability density functions of (a, c) size and (b, d) topographic index of predicted landslides in the CB-MR study area under increasing rainfall intensity and under increasing root strength. Black lines represent the observed landslides. Colored lines represent the predictions using the different parameterizations. Figures 14a and 14b show the distributions for the simulations with increasing rainfall intensity and other values from the base case parameterization ($\phi = 40°$, $C_{r0} = 22$ kPa), while Figures 14c and 14d show the distributions for the simulations with increasing root strength, friction angle from the base case parameterization ($\phi = 40°$), and 8 mm/h rainfall intensity. Note the different vertical scales in the four panels.

location's landslide history. This history is absent from our soil depth submodel, which assumes 6000 years of uninterrupted colluvial fill, resulting in overprediction of landslide abundance. Furthermore, this submodel does not account for other stochastic processes such as tree throw and animal burrowing that can result in locally high soil depth variability [*Schmidt*, 1999; *Heimsath et al*., 2001], which can in turn affect slope stability. Exfiltration from bedrock and drainage from ridge-top roads, which cannot be captured by our hydrological model, are known to be important in triggering landslides in this area [*Montgomery et al*., 2000, 2009]. Similarly, root strength is known to vary not only with soil depth but also between vegetation types, ages (or time since death), and locations across the landscape [e.g., *Wu and Sidle*, 1995; *Schmidt et al*., 2001; *Dhakal and Sidle*, 2003; *Roering et al*., 2003; *Hales et al*., 2009]. Moreover, in analyzing the cumulative impact of the storm series on the landscape, we consider only new landslides caused by each storm but we neglect to consider changes to the landscape that result from failures in previous storms, which could include variations in soil depth, vegetation, and hydrologic properties.

Comparing modeled and field-based observations at the CB-1 site illustrates these effects (Figure 16). The CB-MR LiDAR data were collected after the CB-1 landslide had occurred leaving a topographic depression, as can be noted by comparing Figures 16a and 16c (prefailure) to Figures 16b and 16d (postfailure); this causes stronger convergence of soil flux in the soil depth submodel, and thus thicker soils downslope of the landslide scar (Figure 16d). The modeled pore pressure pattern is topographically driven (Figure 16b) and cannot capture pore pressure spikes in the field-measured data due to local exfiltration (Figure 16a). These differences affect the resulting predictions as can be observed by comparing the application of the search algorithm to the CB-1 site using field-based observations [*Bellugi et al*., 2015] with those from the application of the algorithm to the larger CB-MR area (this study). While in both applications the search algorithm predicts landslides centered on the area of high pore pressure and thicker soils, predicted landslides have a very different size and shape (Figure 16).

The difference in mapped landslides between the *Montgomery et al*. [2000] landslide inventory (Figures 16b and 16d) and the field survey of *Montgomery et al*. [2009] (Figures 16a and 16c) reflects the mapping uncertainty

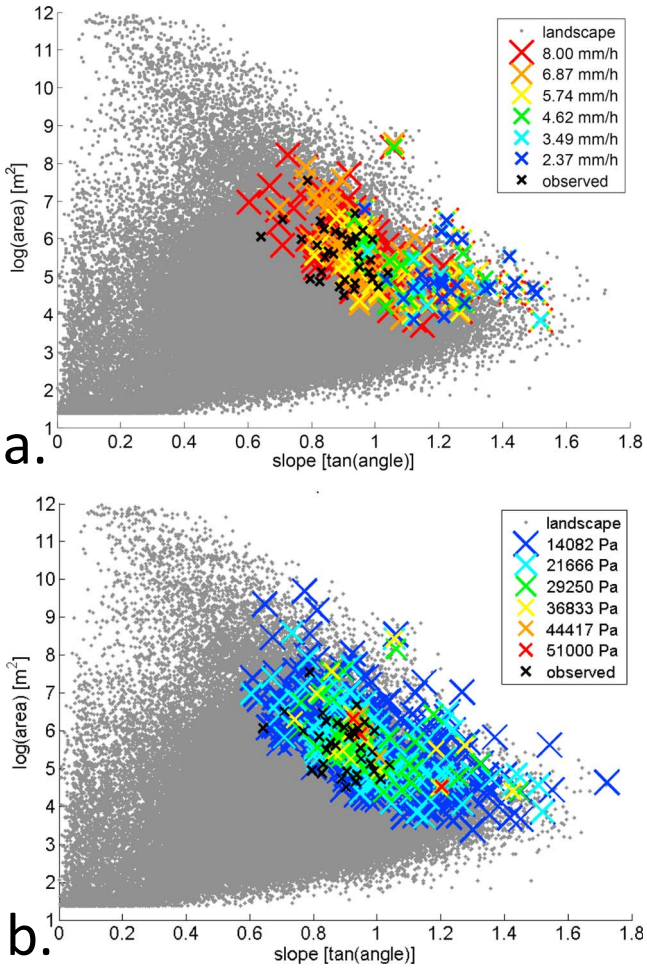

Figure 15. Area-slope scatterplot of predicted landslides in the CB-MR study area (a) under increasing rainfall intensity and (b) under increasing root strength. Black symbols represent the observed landslides. Colored symbols represent the predictions using the different parameterizations. The other parameters in Figure 15a are from the base case parameterization ($\phi = 40°$, $C_{r0} = 22$ kPa), while in Figure 15b the friction angle is from the base case parameterization ($\phi = 40°$), and rainfall intensity is 8 mm/h. Note that markers are differently sized to show overlap.

for this inventory, reported as ~5 m [*Montgomery and Dietrich*, 1994]. This uncertainty both influences landslide location and introduces a size bias, since scars were mapped larger than they were observed in the field [*Montgomery and Dietrich*, 1994]. This may partly explain why predicted landslides are on average 85% smaller than observed. A further size bias is introduced by the omission of some of the smaller landslides reported in previous work in the area [*Montgomery*, 1991, 1994].

MD-STAB incorrectly predicts that many of the observed landslides should be stable, suggesting that it overestimates their resistances (section 6.2.7). This may be due to overestimation of the landslides' perimeters but not their areas in a grid-based discretization. Alternative meshes could reduce discretization problems, though these would need symmetric topology since the search algorithm requires symmetric matrices. The overestimate may also be due to MD-STAB's assumption of hydrostatic conditions on the upslope and downslope wedges, when in reality slope-parallel seepage should reduce the resistance on these boundaries [*Milledge et al.*, 2014]. We are not aware of a suitable earth pressure treatment that can account for slope-parallel seepage.

Attempts to predict landslides over an extended period of time are further complicated by uncertainty in landslide-triggering storm characteristics. We tested two very different approaches: a composite series comprising basic (boxcar) representations of all the landslide-triggering storms and a detailed (10 min) time series for the largest storm. We expected the size and location of predicted landslides to differ between approaches, because (1) the longer duration of the detailed time series can result in slightly different hydrologic conditions than its boxcar representation (Figure 4) and (2) in the composite series we attribute landslides to the first storm that causes that location to fail, which is dependent on both model parameters and the storm sequence. However, the different approaches did not result in large differences in predicted location (Figure 5) or size (Figure 8), other than a small shift down the hollow axis using the detailed time series (Figure 8b). This shift is attributable to the larger extent of wet areas in the longer hydrological simulation. The similarities between the two approaches suggest that a simplified representation of storm events may be sufficient to explore the effect of changing storm intensity-duration-frequency on landslide response.

Both storm representation approaches result in a slightly broader range of landslide sizes than observed (Figure 8a), perhaps reflecting incompleteness of the observational data set or overestimates in resistance in MD-STAB (both discussed above). The composite simulations predict that landslides are contributed only by storms 1 and 6 (the second largest and the largest of the series, respectively), which is inconsistent with

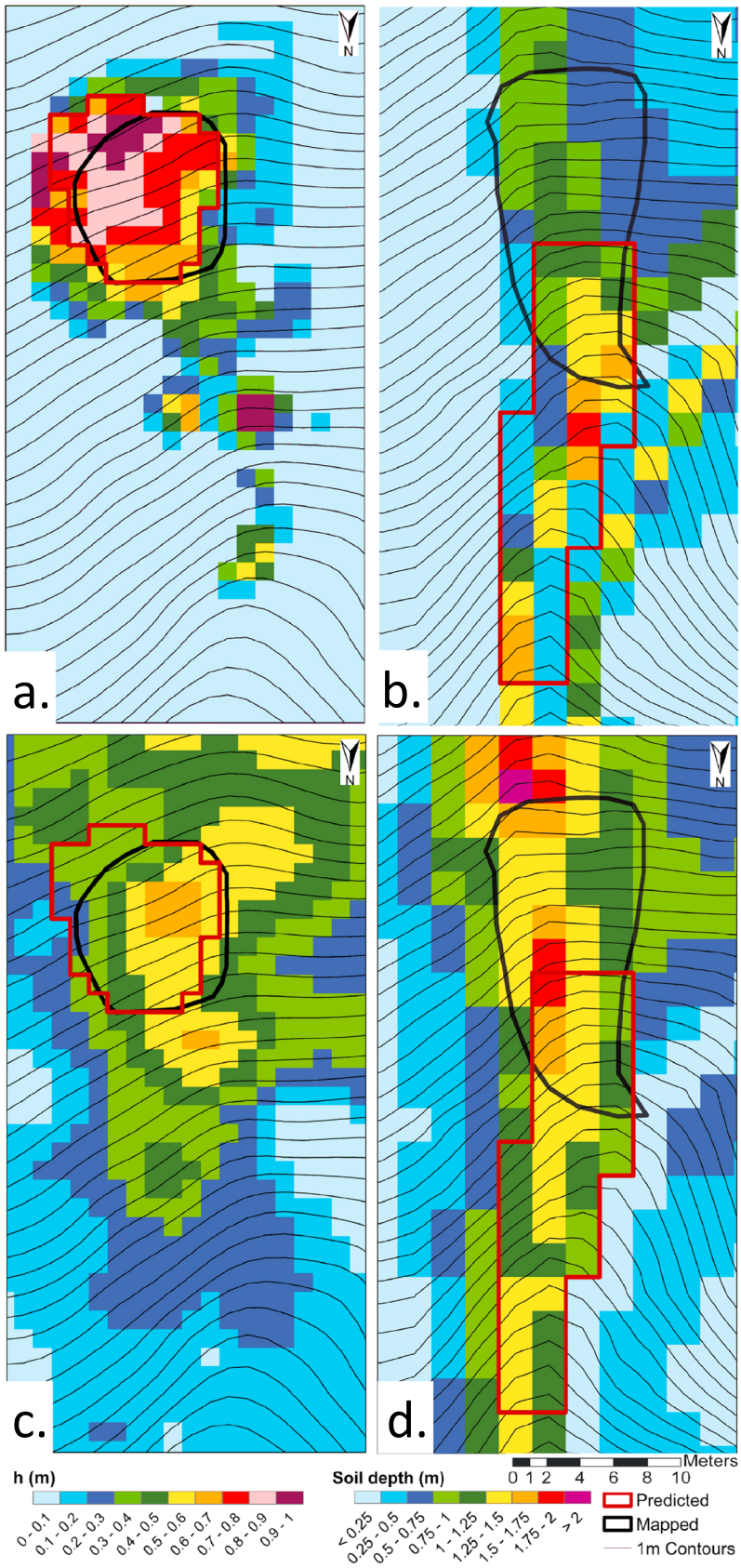
a.
b.
c.
d.
N
h (m)
0 - 0.1
0.1 - 0.2
0.2 - 0.3
0.3 - 0.4
0.4 - 0.5
0.5 - 0.6
0.6 - 0.7
0.7 - 0.8
0.8 - 0.9
0.9 - 1
Soil depth (m)
< 0.25
0.25 - 0.5
0.5 - 0.75
0.75 - 1
1 - 1.25
1.25 - 1.5
1.5 - 1.75
1.75 - 2
> 2
Meters
0 1 2 4 6 8 10
Predicted
Mapped
1m Contours

Figure 16

observations. This is because locations that can fail in the lower intensity storms 2–5 have already failed in storm 1, while stable locations in storm 1 will remain stable in storms 2–5 (but may fail in storm 6). A different ordering of the boxcar storms changes the attribution of individual landslides to individual storms. For example, with the largest storm first, subsequent storms trigger no new landslides. However, reordering the storm sequence in ascending or descending order of rainfall intensity results in (1) the same number of landslides and of hits (defined as predictions overlapping observations) as the historical sequence and (2) size and location distributions that are indistinguishable at the 99.99% confidence level by a K-S test. In reality, spatiotemporal variations of rainfall or other catchment properties (e.g., antecedent moisture, vegetation state, and soil depth) could cause sites that were stable in a more intense storm to fail in a less intense subsequent storm.

7.2. Comparison to Other Models

Ideally, we would compare our model with other discrete landslide models at the same study area. However, no other discrete landslide model has been applied at this site. Instead, we discuss the differences in approach between our model and other discrete models and then compare our predictions with the infinite-slope models that have been applied to this landscape to predict landslide susceptibility.

7.2.1. Discrete Landslide Models

To our knowledge only three other models capable of predicting discrete shallow landslides have been applied at the catchment scale [*Qiu et al*., 2007; *Mergili et al*., 2014; *Von Ruette et al*., 2013]. These models, like ours, require spatial soil depth, root strength, and pore pressure data, though each study differs in how these parameters are calculated and more fundamentally in their model structure.

In common with our approach, *Qiu et al*. [2007] and *Mergili et al*. [2014] both use *Hovland's* [1977] three-dimensional limit equilibrium model to test the stability of discrete shapes. However, their approach differs in two respects: (1) rather than a repeatable deterministic search assuming failure at the soil-bedrock interface, they use a Monte Carlo based search and allow failure within the soil and in some cases bedrock. They apply Hovland's method [*Hovland*, 1977] without accounting for lateral resistance on the unstable block and thus underestimate the factor of safety [*Chen and Chameau*, 1983]. Testing their model at a 0.2 km^2 site in Japan, *Qiu et al*. [2007] found one observed landslide coincident with their predictions but did not perform a systematic comparison with a landslide inventory.

In common with our approach, *Von Ruette et al*. [2013] represent lateral resistance on the margins of clusters of unstable cells. However, they represent shallow landslide mechanics as a cascade of failures with cells failing sequentially rather than simultaneously as in the conventional limit equilibrium framework. At present it remains unclear whether one approach is a consistently better approximation of the true landslide mechanics. Modeling sequential failure removes the need for a search algorithm but requires an iterative solution; reported run times suggest a comparable computational cost to that of our search algorithm.

Our model also differs from that of *Von Ruette et al*. [2013] in its treatment of the forces acting on the soil columns. In their model, root cohesion acts only on the upslope and cross-slope column boundaries, not the base or downslope boundaries, and is depth invariant. They do not account for passive resistance on the downslope boundary and assume that resistance on this boundary is independent of slope. *Von Ruette et al*. [2013] neglect friction on the cross-slope boundaries and assume both compressive and tensile lateral resistance to be mostly due to soil suction. This may not be appropriate for soils such as those found in our field site, where hydraulic conductivity is an order of magnitude higher than that for soils in their study area [*Ebel et al*., 2007b]. Using parameters calibrated from a nearby site, *Von Ruette et al*. [2013] reproduced the general size-frequency distribution of observed landslides but overpredicted the number of landslides by 38%, on average; their volume by 85%, on average; their slope angle (50° on average compared with 29° observed); and the percentage of landslides in forest (78% compared with 38% observed).

Figure 16. Comparison of predictions and observations at the CB-1 landslide. In Figures 16b and 16c the search algorithm is parameterized with the field-measured data reported in *Montgomery et al*. [2009] and *Bellugi et al*. [2015], while in Figures 16b and 16d it is parameterized using modeled data (this study) and the landslide data set reported by *Montgomery et al*. [2000]. Topographic data in Figures 16a and 16c derive from a prefailure total station survey, while those in Figures 16b and 16d are derived from a postfailure LiDAR survey. Shown are the (a) actual and (b) modeled water table heights (h) at the time of failure and the (c) actual and (d) modeled prefailure soil depth.

7.2.2. Models Applied to CB-MR

Using the same 2 m topographic data used here and the coupled slope stability and steady state hydrological model SHALSTAB [*Montgomery and Dietrich*, 1994], predictions overlapped all landslides with 20% of the study area classified as unstable [*Dietrich et al*., 2001]. *Montgomery et al*. [2000] modified this model to account for additional lateral resistance based on an assumed landslide geometry (and constant soil depth) and outperformed the random-placement model by 3:1. Our application of the infinite-slope model with spatially variable soil depth and a dynamic hydrological model slightly improves model performance, overlapping all landslides with only 17% of the study area classified as unstable, compared to 2% recorded landslide area.

In comparison, our model predictions using the search algorithm overlap 56% of the landslides with 4% of the landscape classified as unstable using the composite storms, 65% of the landslides with 5% of the landscape classified as unstable using the 1996 storm, and outperforms the random-placement model by 6:1 and 8:1, respectively. Relative to infinite-slope applications, our model has more false negatives and fewer false positives.

Reduced false positives are consistent with the inclusion of lateral resistance in the method of *Bellugi et al*. [2015] with our parameterization. The infinite-slope method neglects this resistance, underestimating resistive forces and thus overpredicting unstable areas. Accounting for lateral resistance by assuming that every cell fails as an individual landslide, as has been suggested by *Anagnostopoulos et al*. [2015], is equally problematic in this study area, vastly underpredicting unstable areas (19 cells or 0.01% of the study area).

The common solution to the infinite-slope model's underestimate of resistance is to inflate one of the strength parameters either based on an expected landslide size, its perimeter area and thus additional lateral resistance [e.g., *Montgomery et al*., 2000], or by setting a soil strength parameter to an "effective" value to counteract a known process inadequacy [e.g., *Montgomery and Dietrich*, 1994]. Under such alternative parameter sets the infinite-slope model performs well, especially once spatial variability in soil depth is included (Figure 11). The infinite-slope model underestimates resistive forces to such an extent that even without any rainfall, predictions can overlap 100% of the landslides with 14% of the landscape predicted as unstable. Our model instead correctly predicts no failure without any rainfall.

Using alternative parameterizations to the base case (Figure 11), our model captures 100% of the landslides with 13% of the landscape predicted as unstable (when $C_{r0} = 11$ kPa, and $\phi = 35°$). Thus, in terms of landslide susceptibility, our predictions do not significantly improve upon existing infinite-slope models other than to narrow the gap between measured and effective soil strength parameters. If susceptibility alone is the goal and there is adequate training data (a landslide inventory) to constrain effective strength parameters, then the simple infinite-slope model may be sufficient. However, where prediction of landslide size as well as location is necessary, increased model dimensionality is required.

7.3. Root Cohesion and Storm Intensity Controls on Landslide Abundance, Size, and Location

More intense rainstorms increase pore water pressure, reducing effective normal stress and thus soil strength, while increased root cohesion increases soil strength. As a result, our model predicts that increased rainfall intensity increases landslide abundance while increased root cohesion reduces landslide abundance. This is consistent with observations in both cases (e.g., *Swanston* [1970], *Selby* [1976], *Moser* [1980], *Cannon and Ellen* [1985], *Wieczorek* [1987], *Ellen and Wieczorek* [1988], *Moser and Schoger* [1989], *Fazarinc and Mikos* [1992], *Wilson and Wieczorek* [1995], *Rickli and Graf* [2009], and reviews in *Wieczorek and Glade* [2005] and *Sidle and Ochiai* [2006]).

Changes to rainfall intensity and cohesion also affect the location and size of landslides. Location changes are fairly subtle in this landscape, with landslides remaining in the hollows in almost all cases, including in the observations. This is because, as suggested by *Dietrich and Dunne* [1978], instability at a site increases as soils thicken and root penetration into bedrock decreases, and therefore failure should be most likely at sites where soil thickness progressively increases and where recurrent high pore pressures are produced [*Reneau and Dietrich*, 1987a]. In this landscape these conditions occur almost exclusively in hollows, where topographically induced convergence of soils and shallow groundwater flow occur. Moderately divergent areas that can be highly saturated due to their thin soil cover (Figure 4) are predicted to be stable (Figure 5), because the effect of root strength is also more pronounced in thin soils. This is consistent with

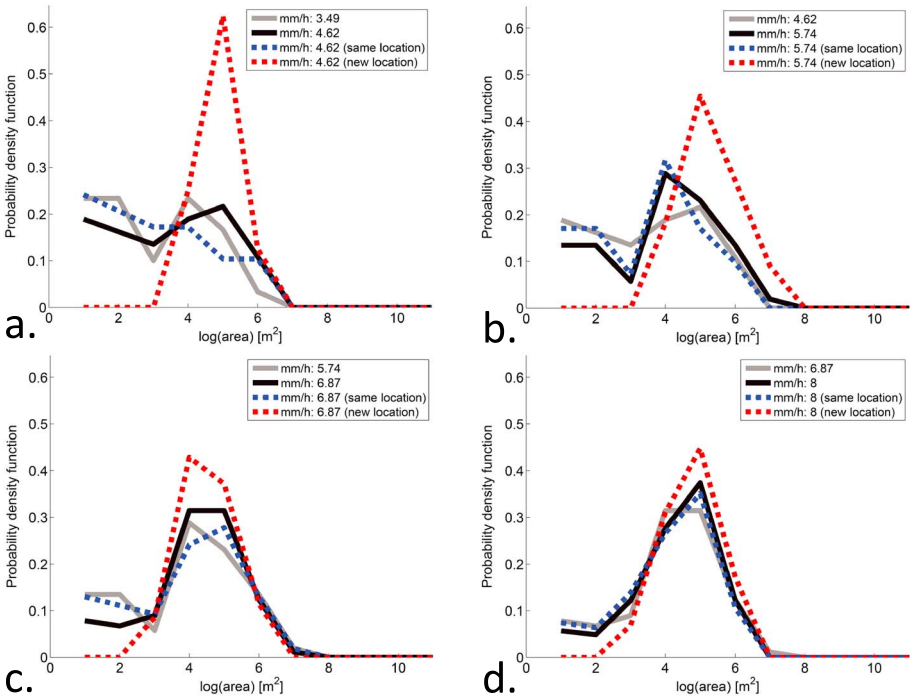

Figure 17. Probability density function of size of predicted landslides in the CB-MR study area for consecutive pairs of storms from the increasing rainfall intensity simulations (and $\varphi = 40°$, $C_{r0} = 22$ kPa). Gray lines and black lines represent the size distributions for the lower intensity and higher-intensity storms, respectively. The dashed blue line is the size distribution of landslides common to both storms, while the dashed red line is the size distribution of landslides only occurring in the higher-intensity storm. Note that while common landslides can decrease or increase in size, new landslides are consistently larger in the higher-intensity storm. Consecutive pairs of rainfall intensities are (a) 3.49–4.62 mm/h, (b) 4.62–5.74 mm/h, (c) 5.74–6.87 mm/h, and (d) 6.87–8.0 mm/h. A similar trend is observed for the pair with 2.37–3.49 mm/h intensity (not shown).

the observed landslide inventory and suggests that the interplay between soil depth, soil saturation, and root strength is a primary control on instability in these landscapes. Increasing rainfall intensity causes landslides to shift down the hollow axis to locations with lower slope but higher upslope area. This reflects the failure of locations where slope angles (and therefore driving forces) were previously too low to fail but, with increased pore water pressure (and therefore reduced resisting force), become unstable. Of these lower slope locations only those with high upslope area are susceptible to failure under increased rainfall intensity (Figure 15a) because their pore water pressure response is strongest. With increasing root cohesion, landslide locations become increasingly clustered in slope-area space (Figure 15b). This reflects landslide locations being constrained to areas of deepest soil, where the stabilizing influence of basal and lateral root cohesion is reduced.

Changes to landslide size (in terms of scar area) are more pronounced than changes to location, with mean area increasing by a factor of 7 in response to either a factor of 3 increase in rainfall intensity or a factor of 4 increase in root cohesion. Increasing storm intensity causes a positive shift in landslide size distribution due to an increase in medium- and larger-sized landslides. This is mainly due to larger landslides occurring in previously stable locations rather than an increase in the sizes of landslides at previously unstable locations (Figure 17). Increased rainfall intensity can trigger failure by either increasing pore pressure over a given area [*Reneau and Dietrich*, 1987a] or expanding the area of a patch of elevated pore pressure [*Casadei et al*., 2003; *Milledge et al*., 2014]. The former mechanism should generate smaller landslides while the latter larger landslides. Our model predictions suggest that in sites that were unstable under lower rainfall intensity, increased pore pressure often results in smaller landslides, while in sites that were previously stable, new failures are generally larger (Figure 17). This is because sites that were previously stable are in relatively strong areas of thinner soils (and thus increased root cohesion) or of lower slope (Figure 15). Because of the greater strength, a larger area must fail collectively to overcome the increased resistance. The addition of new larger landslides dominates the change in the distribution (Figure 14), resulting in an increased average size. To our

knowledge there has not been an attempt to compare size distributions for different rainfall intensities, though our results suggest that such data might provide insight into hydrological process and in particular pore pressure dynamics responsible for triggering shallow landslides. Such an analysis would be complicated in practice by the spatial variability in rainfall intensity in any given storm event.

Increasing root cohesion causes a right shift in landslide size distribution, consistent with many observations on landslide size for different vegetation types [*Moser*, 1971; *Selby*, 1976; *Lehre*, 1982; *Moser and Schoger*, 1989; *Gabet and Dunne*, 2003; *Rickli and Graf*, 2009]. This is expected since, as suggested by *Reneau and Dietrich* [1987a], landslides need a larger volume to surface area ratio as the resistance per unit surface area increases due to increased cohesion. Both the landslides in areas that were unstable under higher root cohesion and those in new unstable areas tend to get smaller with decreasing root cohesion. Because of the lower root strength, a smaller area is required to overcome the reduced resistance.

7.4. Applicability to Other Landscapes

Section 7.1 demonstrates the sensitivity of model performance to input data quality even at a well-studied site like CB-MR. Parameters can be calibrated to observations, but this requires accurate landslide mapping, which is difficult to obtain; and calibrating at one location does not necessarily improve the performance at another. Instead, we have parameterized the model using observations within the study area and simplified process-based models, reserving landslide observations as a test of the model. Where calibration is necessary, modeling landslide size as well as location introduces a second set of predictions that can be compared to observations for calibration.

Application to a different area would require a comparable effort to constrain relevant parameters such as soil depth, root strength, friction angle, and hydraulic conductivity. Our results suggest that soil depth and pore pressure are key parameters to constrain (Figure 16). Both are difficult to model: soil depth because it depends on the history of previous landsliding; and pore water pressure because it is strongly controlled by local nontopographic factors.

Different landscapes may also require alternative submodels for soil depth, root strength, and pore pressure. For example, in some landscapes where topography lacks a regular division into hollows and noses, landslides occur on more planar slopes (e.g., review in *Reneau and Dietrich* [1987b]). In highly dissected landscapes such as the Oregon Coast Range, topography concentrates subsurface flow even in the presence of fractures and other material heterogeneities [e.g., *Montgomery et al*., 1997]. In other less dissected landscapes these heterogeneities more strongly affect subsurface flow pathways and thus pore pressure patterns, in which case other hydrologic models that focus on vertical infiltration or that treat flow in three dimensions [e.g., *Simoni et al*., 2008; *Baum et al*., 2010] would be more appropriate. Though we did not adopt such models in our study, our approach is fully compatible with them. Detailed data collection is the principal limitation on regional-scale applications of our approach. Nevertheless, our experience suggests that the parameterization can be considerably improved using regionally calibrated submodels and by noting soil depth and root strength in a subsample of landslides in the landscape of interest. Otherwise, our approach could be applied to large areas, as its scalability makes it well suited for use on high-performance computing platforms [*Bellugi et al*., 2015].

8. Conclusions

We combine a model that predicts discrete shallow landslides [*Milledge et al*., 2014; *Bellugi et al*., 2015] with process-based submodels to estimate soil depth, root strength, and pore water pressure. This approach is tested by comparing predicted shallow landslides with mapped sites over 10 years in a 0.5 km^2 study area in the Oregon Coast Range. Metrics of performance include the following: (i) the percent of hits (defined as predictions overlapping observations) relative to a random model, (ii) size and location distributions of observed and predicted landslides, and (iii) the size of individual predicted and observed landslides where they overlap. In this landscape both observed and predicted landslides predominantly occur in hollows (where topographic convergence leads to thicker soils, reducing root cohesion); where slopes are steep, increasing driving force and reducing basal resistance; and where drainage areas are large, increasing pore pressures and reducing soil strength. Without calibration the model predictions overlap 65% of observed landslides (compared to 11% with a random-placement model), more than 95% of the stable area is correctly

predicted, and less than 5% of the landscape is predicted to be unstable (compared to 2% recorded landslide area). Our approach broadly captures observed landslide size and location distributions but with a slightly wider range of topographic locations, too many small landslides, and slightly smaller average landslide size. Thirteen percent of locations where predicted and observed landslides overlap have predicted landslide size within a factor of 1.25 of the observed, 28% have sizes within a factor of 1.5, 45% have sizes within a factor of 1.75, and 55% have sizes within a factor of 2.

Moderate changes in model parameters (±5° in friction angle, ±20 mm/h in maximum storm intensity, or ±10 kPa in maximum root strength) result in large changes in model performance (0–100% hits and 0–13% unstable area), highlighting the importance of good field-derived parameter estimates. In all the simulations performed, missed landslides are the result of mapping errors or of errors in parameterization of the slope stability model of *Milledge et al*. [2014] rather than failures of the search algorithm of *Bellugi et al*. [2015]. For a well-parameterized site the model accurately predicts landslide location and size. When the parameters are less constrained the model reproduces the general behavior but fails to reproduce specifics with the same accuracy.

An identically parameterized infinite-slope model overlaps all observed landslides but predicts a much larger unstable area (~30%). This overprediction can be reduced by using effective parameters, allowing the infinite-slope model to perform as well as our more complex model at delineating areas of high landslide susceptibility. However, our model improves process representation by representing the forces acting on all the margins of an unstable block rather than only the base, reducing the reliance on effective parameters (e.g., for friction angle, storm intensity, or root strength). Most importantly, our model makes it possible to predict not only the susceptibility of a given location but also landslide size (and thus initial sediment volume) by testing the stability of discrete landslides, clarifying how heterogeneous landscape properties affect landslide size and location.

In particular, we explore the effects of varying rainfall intensity and root cohesion. Increased storm intensity increases the magnitude and lateral extent of elevated pore pressure and the number of landslides. This spread of elevated pore pressure then destabilizes relatively strong areas of thinner soils or reduced slope. Because of the greater strength, larger areas must fail collectively to overcome the marginal resistance. Hence, landslide size increases with rainfall intensity. Under increased rainfall intensity landslides are also predicted to occur farther downslope along the axes of unchanneled valleys (hollows). This occurs because these lower hollow areas are generally less steep and thus require more runoff to be destabilized. With increasing root cohesion landslides decrease in number but increase in average size and volume to overcome the additional resistance. Locations are increasingly constrained to areas that have both deep soils and remain steep, typically found in the middle of hollows, resulting in a narrower location distribution.

Our findings suggest that shallow landslide abundance, location, and size are ultimately controlled by covarying landscape properties such as slope, pore pressure, root strength, and soil depth. The greatest challenge to generating accurate predictions remains the estimation of time-and-space-varying root strength, pore pressure, and, perhaps most importantly, soil depth, across a landscape.

Notation

Variable Description, Units

- A drainage area, m^2.
- C_b root cohesion at the basal failure surface, Pa.
- C_{r0} root cohesion at the surface, Pa.
- C_b root cohesion at the basal failure surface, Pa.
- C_l depth-averaged lateral root cohesion, Pa.
- D soil diffusion coefficient, m^2/yr.
- F_d downslope driving force, N.
- FS factor of safety.
- F_w central block weight force, N.
- I_T topographic index, m.

K hydraulic conductivity, m/d.
K_0 coefficient of at-rest earth pressure.
K_a active earth pressure coefficient.
K_p passive earth pressure coefficient.
R_b basal shear resisting force, N.
R_d net downslope resisting force (passive), N.
R_l, R_r, cross-slope shear resisting force, N.
R_u net upslope driving force (active), N.
S_c critical slope angle.
S_r soil degree of saturation.
T hydraulic transmissivity, m^2/d.
b grid cell size, m.
h_i height of the saturated fraction at time step i, m.
j the reciprocal of the e-folding depth of C_b, 1/m.
l length of the slide block, m.
m saturation ratio.
q_i effective precipitation at time step i, m/d.
t soil production time interval, years.
t_i duration of time step i, days.
v soil void ratio.
w width of the slide block, m.
z failure surface depth below the ground surface, m.
z_b height of soil-bedrock boundary above reference datum, m.
z_c vertical coordinate within soil column, m.
z_t topographic elevation above reference datum, m.
z_w water table depth below the ground surface, m.
α soil production rate constant, 1/m.
γ_s unit weight of the soil, $N\,m^{-3}$.
γ_w unit weight of water, $N\,m^{-3}$.
ε soil production rate at zero soil thickness, m/yr.
θ slope angle, degrees.
λ eigenvalue.
λ^* smallest nonzero eigenvalue.
ρ_s bulk density of soil, $kg\,m^{-3}$.
ρ_w bulk density of water, $kg\,m^{-3}$.
ϕ soil friction angle, degrees.
$\mathbf{F}$ force matrix, N.
$\mathbf{R}$ resistance matrix, N.
$\mathbf{q}$ soil flux per unit contour width.
$\mathbf{x}$ discrete indicator vector.
$\mathbf{y}$ eigenvector.
$\mathbf{y}^*$ Eigenvector corresponding to λ^*.

Acknowledgments
This research was financially supported by grants from the United States Forest Service (09-JV-11221634-233), NSF (NSF-EAR-0828047), NASA (ROSES 09-IDS09-0049), and NERC (NER/S/A/2004/12248). We thank Kevin Schmidt for providing root cohesion and soil depth data, Dave Montgomery for providing landslide dimensions data, and Maria Cristina Rulli for providing assistance with the hydrological modeling. All data sets used in this study have been previously published, please see citations in the text. Reviews by Alex Densmore, John Buffington, Katerina Michaelides, Oliver Korup, and four anonymous referees considerably improved this manuscript.

References

Anagnostopoulos, G. G., S. Fatichi, and P. Burlando (2015), An advanced process-based distributed model for the investigation of rainfall-induced landslides: The effect of process representation and boundary conditions, *Water Resour. Res.*, *51*, 7501–7523, doi:10.1002/2015WR016909.

Baum, R. L., J. W. Godt, and W. Z. Savage (2010), Estimating the timing and location of shallow rainfall-induced landslides using a model for transient, unsaturated infiltration, *J. Geophys. Res.*, *115*, F03013, doi:10.1029/2009JF001321.

Beguería, S. (2006), Validation and evaluation of predictive models in hazard assessment and risk management, *Nat. Hazards*, *37*(3), 315–329.

Bellugi, D. (2012), What controls shallow landslide size across landscapes?, PhD thesis, Univ. of Calif., Berkeley.

Bellugi, D., D. Milledge, W. E. Dietrich, J. McKean, and J. T. Perron (2015), A spectral clustering search algorithm for predicting shallow landslide size and location, *J. Geophys. Res. Earth Surf.*, *120*, 300–324, doi:10.1002/2014JF003137.

Benda, L. E., and T. W. Cundy (1990), Predicting deposition of debris flows in mountain channels, *Can. Geotech. J.*, *27*, 209–417.

Benda, L. E., and T. Dunne (1997), Stochastic forcing of sediment supply to the channel network form landsliding and debris flow, *Water Resour. Res.*, *33*, 2849–2863, doi:10.1029/97WR02388.
Beven, K., and M. J. Kirkby (1979), A physically based variable contributing area model of basin hydrology, *Hydrol. Sci. Bull.*, *24*, 43–69.
Bishop, A. W. (1955), The use of slip circles in the stability analysis of slopes, *Geotechnique*, *5*, 7–17.
Borga, M., G. Dalla Fontana, and F. Cazorzi (2002), Analysis of topographic and climatic control on rainfall-triggered shallow landsliding using a quasi-dynamic wetness index, *J. Hydrol.*, *268*(1), 56–71.
Borja, R. I., and J. A. White (2010), Continuum deformation and stability analyses of a steep hillside slope under rainfall infiltration, *Acta Geotech.*, *5*, 1–14.
Brien, D. L., and M. E. Reid (2008), Assessing deep-seated landslide susceptibility using 3-D groundwater and slope-stability analyses, southwestern Seattle, Washington, *Rev. Eng. Geol.*, *20*, 83–101.
Cannon, S. H., and S. D. Ellen (1985), Rainfall conditions for abundant debris avalanches in the San Francisco Bay region, California, *Calif. Geol.*, *38*(12), 267–272.
Carr, H., J. Snoeyink, and U. Axen (2003), Computing contour trees in all dimensions, *Comput. Geom.*, *24*(2), 75–94.
Casadei, M., W. E. Dietrich, and N. L. Miller (2003), Testing a model for predicting the timing and location of shallow landslide initiation in soil mantled landscapes, *Earth Surf. Processes Landforms*, *28*, 925–950.
Chen, R. H., and J. L. Chameau (1983), Three-dimensional limit equilibrium analysis of slopes, *Geotechnique*, *33*(1), 31–40.
Chugh, A. K., and J. D. Smart (1981), Suggestions for slope stability calculations, *Comput. Struct.*, *14*(1–2), 43–50, doi:10.1016/0045-7949(81)90082-1.
Chung, C. J. F., and A. G. Fabbri (2003), Validation of spatial prediction models for landslide hazard mapping, *Nat. Hazards*, *30*(3), 451–472.
Claessens, L., G. B. M. Heuvelink, J. M. Schoorl, and A. Veldkamp (2005), DEM resolution effects on shallow landslide hazard and soil redistribution modelling, *Earth Surf. Process. Landforms*, *30*, 461–477, doi:10.1002/esp.1155.
Conover, W. J. (1971), *Practical Nonparametric Statistics*, Wiley, New York.
Corominas, J., et al. (2014), Recommendations for the quantitative analysis of landslide risk, *Bull. Eng. Geol. Environ.*, *73*(2), 209–263, doi:10.1007/s10064-013-0538-8.
Dallal, G. E. (2012), *The Little Handbook of Statistical Practice*, Tuft Univ., Boston, Mass. [Available at www.statisticalpractice.com.]
Dhakal, A. S., and R. C. Sidle (2003), Long-term modelling of landslides for different forest management practices, *Earth Surf. Process. Landforms*, *28*, 853–868, doi:10.1002/esp.499.
Dietrich, W. E., and T. Dunne (1978), Sediment budget for a small catchment in mountainous terrain, *Z. Geomorph. Suppl.*, *29*, 191–206.
Dietrich, W. E., C. J. Wilson, D. R. Montgomery, J. McKean, and R. Bauer (1992), Erosion thresholds and land surface morphology, *Geology*, *20*(8), 675–679.
Dietrich, W. E., R. Reiss, M. Hsu, and D. R. Montgomery (1995), A process-based model for colluvial soil depth and shallow landsliding using digital elevation data, *Hydrol. Processes*, *9*, 383–400.
Dietrich, W. E., D. Bellugi, and R. Real de Asua (2001), Validation of the shallow landslide model SHALSTAB for forest management, in *Land Use and Watersheds: Human Influence on Hydrology and Geomorphology in Urban and Forest Areas*, *AGU Water Sci. Appl.*, vol. 2, edited by M. S. Wigmosta and S. J. Burges, pp. 195–227, AGU, Washinton, D. C., doi:10.1029/WS002.
Dietrich, W. E., D. G. Bellugi, L. S. Sklar, J. D. Stock, A. M. Heimsath, and J. J. Roering (2003), Geomorphic transport Laws for predicting landscape form and dynamics, in *Prediction in Geomorphology*, edited by P. R. Wilcock and R. M. Iverson, AGU, Washington, D. C., doi:10.1029/135GM09.
Dietrich, W. E., J. McKean, D. Bellugi, and T. Perron (2007), The prediction of shallow landslide location and size using a multidimensional landslide analysis in a digital terrain model, in *Proceedings of the Fourth International Conference on Debris Flow Hazards Mitigation: Mechanics, Prediction, and Assessment, Chengdu, China*, pp. 10–13, IOS Press, Amsterdam, Netherlands.
Dunne, T. (1991), Stochastic aspects of the relations between climate, hydrology and landform evolution, *Trans. Jpn. Geomorphol. Union*, *12*, 1–24.
Ebel, B. A., K. Loague, W. E. Dietrich, D. R. Montgomery, R. Torres, S. P. Anderson, and T. W. Giambelluca (2007a), Near-surface hydrologic response for a steep, unchanneled catchment near Coos Bay, Oregon: 1. Sprinkling experiments, *Am. J. Sci.*, *307*, 678–708.
Ebel, B. A., K. Loague, J. E. VanderKwaak, W. E. Dietrich, D. R. Montgomery, R. Torres, and S. P. Anderson (2007b), Near-surface hydrologic response for a steep, unchanneled catchment near Coos Bay, Oregon: 2. Comprehensive physics-based simulations, *Am. J. Sci.*, *07*, 709–748, doi:10.2475/04-2007-03.
Ellen, S. D., and G. F. Wieczorek (1988), Landslides, floods, and marine effects of the storm of January 3–5, 1982, in the San Francisco Bay Region, California, U.S. Geol. Surv. Prof. Pap., 1434.
Fannin, R. J., and M. P. Wise (2001), An empirical-statistical model for debris flow travel distance, *Can. Geotech. J.*, *38*(5), 982–994.
Fawcett, T. (2006), An introduction to ROC analysis, *Pattern Recognit. Lett.*, *27*, 861–874.
Fazarinc, R., and M. Mikos (1992), Feststoffmobilisierung als Folge der extremen Niederschläge in Slowenien, in *Proceedings International Symposium Interpraevent*, vol. 1, pp. 377–388, Bern.
Frattini, P., G. Crosta, and A. Carrara (2010), Techniques for evaluating the performance of landslide susceptibility models, *Eng. Geol.*, *11*, 62–72.
Gabet, E. J., and T. Dunne (2003), A stochastic sediment delivery model for a steep Mediterranean landscape, *Water Resour. Res.*, *39*(9), doi:10.1029/2003WR002341.
Godt, J. W., R. L. Baum, W. Z. Savage, D. Salciarini, W. H. Schulz, and E. L. Harp (2008), Transient deterministic shallow landslide modeling: Requirements for susceptibility and hazard assessments in a GIS framework, *Eng. Geol.*, *102*(3–4), 214–226, doi:10.1016/j.enggeo.2008.03.019.
Guzzetti, F., B. D. Malamud, D. L. Turcotte, and P. Reichenbach (2002), Power-law correlations of landslide areas in central Italy, *Earth Planet. Sci. Lett.*, *195*, 169–183.
Hales, T. C., C. R. Ford, T. Hwang, J. M. Vose, and L. E. Band (2009), Topographic and ecologic controls on root reinforcement, *J. Geophys. Res.*, *114*, F03013, doi:10.1029/2008JF001168.
Hanley, J. A., and B. J. McNeil (1982), The meaning and use of the area under a receiver operating characteristic (ROC) curve, *Radiology*, *143*(1), 29–36.
Head, K. H., and R. J. Epps (2014), Manual of Soil Laboratory Testing, Volume III: Effective Stress Tests, 3rd ed., Whittles, CRC Press LLC, Boca Raton, Fla.
Heimsath, A. M., W. E. Dietrich, K. Nishiizumi, and R. C. Finkel (2001), Stochastic processes of soil production and transport: Erosion rates, topographic variation, and cosmogenic nuclides in the Oregon Coast Range, *Earth Surf. Processes Landforms*, *26*, 531–552.
Horn, R. A., and C. A. Johnson (1985), Matrix Analysis, pp. 176–180, Cambridge Univ. Press, London.
Hovland, H. J. (1977), Three-dimensional slope stability analysis method, *ASCE J. Geotech. Eng. Div.*, *103*(GT9), 971–986.
Hungr, O., S. McDougall, M. Wise, and M. Cullen (2008), Magnitude-frequency relationships of debris flows and debris avalanches in relation to slope relief, *Geomorphology*, *96*(3–4), 355–365.

Iida, T. (1984), A hydrological method of estimation of the topographic effect on the saturated throughflow, *Trans. Jpn. Geomorphol. Union*, *5*(1), 1–12.
Iverson, R. M. (2000), Landslide triggering by rain infiltration, *Water Resour. Res.*, *36*(7), 1897–1910.
Jaky, J. (1944), The coefficient of earth pressure at rest, *J. Union Hung. Eng. Archit.*, *78*(22), 355–358.
Larsen, I. J., D. R. Montgomery, and O. Korup (2010), Landslide erosion controlled by hillslope material, *Nat. Geosci.*, *3*(4), 247–251, doi:10.1038/ngeo776.
Larsen, M. C., and A. Simon (1993), A rainfall intensity-duration threshold for landslides in a humid-tropical environment, Puerto Rico, *Geogr. Ann. Ser. A*, *75*(1–2), 13–23.
Lehmann, P., and D. Or (2012), Hydromechanical triggering of landslides: From progressive local failures to mass release, *Water Resour. Res.*, *48*, W03535, doi:10.1029/2011WR010947.
Lehre, A. K. (1981), Sediment budget of a small California Coast Range drainage basin near San Francisco, in *Erosion and Sediment Transport in Pacific Rim Steeplands*, *Int. Assoc. Hydrol. Sci*, vol. 132, edited by A. R. H. Davies and A. J. Pearce, pp. 123–139, Christchurch, New Zealand.
Lehre, A. K. (1982), Sediment mobilization and production from a small mountain catchment: Lone Tree Creek, Marin County, California, PhD dissertation, Univ. of Calif., Berkeley.
Malamud, B. D., D. L. Turcotte, F. Guzzetti, and P. Reichenbach (2004), Landslide inventories and their statistical properties, *Earth Surf. Processes Landforms*, *29*, 687–711.
Mergili, M., I. Marchesini, M. Rossi, F. Guzzetti, and W. Fellin (2014), Spatially distributed three-dimensional slope stability modelling in a raster GIS, *Geomorphology*, *206*, 178–195.
Milledge, D., D. Bellugi, J. McKean, A. L. Densmore, and W. E. Dietrich (2014), A multi-dimensional stability model for predicting landslide size and shape across landscapes, *J. Geophys. Res. Earth Surf.*, *119*, 2481–2504, doi:10.1002/2014JF003135.
Montgomery, D. R. (1991), Channel initiation and landscape evolution, PhD dissertation, 421 pp., Dep. of Geol. and Geophys., Univ. of Calif., Berkeley.
Montgomery, D. R. (1994), Road surface drainage, channel initiation, and slope instability, *Water Resour. Res.*, *30*(6), 1925–1932, doi:10.1029/94WR00538.
Montgomery, D. R., and W. E. Dietrich (1992), Channel initiation and the problem of landscape scale, *Science*, *255*, 826–830.
Montgomery, D. R., and W. E. Dietrich (1994), A physically-based model for topographic control on shallow landsliding, *Water Resour. Res.*, *30*(4), 1153–1171, doi:10.1029/93WR02979.
Montgomery, D. R., and W. E. Dietrich (1998), Where do channels begin?, *Nature*, *336*, 232–234, doi:10.1038/336232a0.
Montgomery, D. R., and W. E. Dietrich (2002), Runoff generation in a steep, soil-mantled landscape, *Water Resour. Res.*, *38*(9), 1168, doi:10.1029/2001WR000822.
Montgomery, D. R., and W. E. Dietrich (2004), Reply to comment by Richard M. Iverson on "Piezometric response in shallow bedrock at CB1: Implications for runoff generation and shallow landsliding", *Water Resour. Res.*, *40*, W03802, doi:10.1029/2003WR002815.
Montgomery, D. R., W. E. Dietrich, R. Torres, S. P. Anderson, and K. Loague (1997), Hydrologic response of a steep unchanneled valley to natural and applied rainfall, *Water Resour. Res.*, *33*(1), 91–109, doi:10.1029/96WR02985.
Montgomery, D. R., K. M. Schmidt, W. E. Dietrich, and H. M. Greenberg (2000), Forest clearing and regional landsliding in the Pacific Northwest, *Geology*, *28*, 311–314.
Montgomery, D., K. M. Schmidt, W. E. Dietrich, and J. McKean (2009), Instrumental record of debris flow initiation during natural rainfall: Implications for modeling slope stability, *J. Geophys. Res.*, *114*, F01031, doi:10.1029/2008JF001078.
Moore, I. D., E. M. O'Loughlin, and G. J. Burch (1988), A contour-based topographic model for hydrological and ecological applications, *Earth Surf. Processes Landforms*, *13*, 305–320.
Moser, M. (1971), Einfluss der Pflanzendecke bei Elementarereignissen auf Grosse und Anzahl der Anbruchsflachen im Bereich des mittleren Lesachtales/Karnten, Centralbl Gesamte Forstwesen.
Moser, M. (1980), Zur Analyse von Hangbewegungen in schwachbindigen bis rolligen Lockergesteinen im alpinen Raum anlässlich von Starkniederschlägen, in *Proc. Int. Symp. Interpraevent*, pp. 121–148.
Moser, M., and H. Schoger (1989), Die Analyse der Hangbewegungen im mittleren Inntal anlässlich der Unwetterkatastrophe 1985, *Wildbach-und Lawinenverbau*, *531*(10), 1–22.
Okimura, T. (1994), Prediction of the shape of a shallow failure on a mountain slope: The three-dimensional multi-planar sliding surface method, *Geomorphology*, *9*, 223–233.
O'Loughlin, E. M. (1986), Prediction of surface saturation zones in natural catchments by topographic analysis, *Water Resour. Res.*, *22*, 794–804, doi:10.1029/WR022i005p00794.
Pack, R. T., D. G. Tarboton, and C. N. Goodwin (1998), The SINMAP Approach to Terrain Stability Mapping, in *Proceedings, International Congress of the International Association for Engineering Geology and the Environment 8*, vol. 8, edited by D. P. Moore and O. Hungr, pp. 1157–1165, A. A. Balkema, Rotterdam, Netherlands.
Pack, R. T., D. G. Tarboton, and C. N. Goodwin (1998), The SINMAP approach to terrain stability mapping, in *Proceedings of 8th Congress of the International Association of Engineering Geology*, pp. 1157–1165, Vancouver, British Columbia, Canada.
Qiu, C., T. Esaki, M. Xie, Y. Mitani, and C. Wang (2007), Spatio-temporal estimation of shallow landslide hazard triggered by rainfall using a three-dimensional model, *Environ. Geol.*, *52*(8), 1569–1579.
Reid, M. E., S. B. Christian, and D. L. Brien (2000), Gravitational stability of three-dimensional stratovolcano edifices, *J. Geophys. Res.*, *105*, 6043–6056, doi:10.1029/1999JB900310.
Reneau, S. L., and W. E. Dietrich (1987a), Size and location of colluvial landslides in a steep forested landscape, *IAHS AISH Publ.*, *165*, 39–48.
Reneau, S. L., and W. E. Dietrich (1987b), The importance of hollows in debris flow studies; examples from Marin County, California, in *Debris Flows/Avalanches: Process, Recognition and Mitigation*, *Rev. Eng. Geol.*, vol. 7, edited by J. E. Costa and G. F. Wiezcorek, pp. 165–180, Geol. Soc. Am., Boulder, Colo.
Rice, R. M., and G. T. B. Foggin (1971), Effect of high intensity storms on soil slippage on mountainous watersheds in southern California, *Water Resour. Res.*, *7*, 1485–1496, doi:10.1029/WR007i006p01485.
Rickli, C., and Graf, F. (2009), Effects of forests on shallow landslides—Case studies in Switzerland, *For. Snow Landscape Res.*, *82*(1), 33—44.
Robison, E. G., K. Mills, J. Paul, L. Dent, and A. Skaugset (1999), Oregon Department of Forestry storm impacts and landslides of 1996, Final Rep., Oregon Department of Forestry, Forest Practices Tech. Rep., 4.
Roering, J. J. (2008), How well can hillslope evolution models "explain" topography? Simulating soil transport and production with high resolution topographic data, *Geol. Soc. Am. Bull.*, *120*, 1248–1262.
Roering, J. J., J. W. Kirchner, and W. E. Dietrich (1999), Evidence for non-linear, diffusive sediment transport on hillslopes and implications for landscape morphology, *Water Resour. Res.*, *35*, 853–870, doi:10.1029/1998WR900090.
Roering, J. J., K. M. Schmidt, J. D. Stock, W. E. Dietrich, and D. R. Montgomery (2003), Shallow landsliding, root reinforcement, and the spatial distribution of trees in the Oregon Coast Range, *Can. Geotech. J.*, *40*(2), 237–253.

Rosso, R., M. C. Rulli, and G. Vannucchi (2006), A physically based model for the hydrologic control on shallow landsliding, *Water Resour. Res.*, *42*, W06410, doi:10.1029/2005WR004369.
Saito, H., O. Korup, T. Uchida, S. Hayashi, and T. Oguchi (2014), Rainfall conditions, typhoon frequency, and contemporary landslide erosion in Japan, *Geology*, *42*(11), 999–1002.
Schmidt, K. M. (1999), Root strength, colluvial soil depth, and colluvial transport on landslide-prone hillslopes, PhD thesis, Univ. of Washington, Seattle, Wash.
Schmidt, K. M., J. J. Roering, J. D. Stock, W. E. Dietrich, D. R. Montgomery, and T. Schaub (2001), Root cohesion variability and shallow landslide susceptibility in the Oregon Coast Range, *Can. Geotech. J.*, *38*(1), 995–1024.
Schwarz, M., D. Cohen, and D. Or (2010), Root-soil mechanical interactions during pullout and failure of root bundles, *J. Geophys. Res.*, *115*, F04035, doi:10.1029/2009JF001603.
Selby, M. J. (1976), Slope erosion due to extreme rainfall: A case study from New Zealand, *Geogr. Ann., Ser. A*, *58*(3), 131–138.
Shi, J., and J. Malik (2000), Normalized cuts and image segmentation, *IEEE Trans. Pattern Anal. Mach. Intell.*, *22*(8), 888–905, doi:10.1109/34.868688.
Sidle, R. C. (1992), A theoretical model of the effects of timber harvesting on slope stability, *Water Resour. Res.*, *28*, 1897–1910, doi:10.1029/92WR00804.
Sidle, R. C., and M. Chigira (2004), Landslides and debris flows strike Kyushu, Japan, *Eos Trans. AGU*, *85*(15), 145–151, doi:10.1029/2004EO150001.
Sidle, R. C., and H. Ochiai (2006), *Landslides: Processes, Prediction, and Land Use*, *Water Resour. Monogr.*, vol. 18, 312 pp., AGU, Washington, D. C.
Simoni, S., F. Zanotti, G. Bertoldi, and R. Rigon (2008), Modelling the probability of occurrence of shallow landslides and channelized debris flows using GEOtop-FS, *Hydrol. Processes*, *22*(4), 532–545.
Soubra, A. H., and B. Macuh (2002), Active and passive earth pressure coefficients by a kinematical approach, Proceedings of the Institution of Civil Engineers, *Geotech. Eng.*, *155*(2), 119–131.
Spowart, J. E., B. Maruyama, and D. B. Miracle (2001), Multi-scale characterization of spatially heterogeneous systems: Implications for discontinuously reinforced metal matrix composite microstructures, *Mater. Sci. Eng., A*, *307*, 51–66.
Stark, C. P., and F. Guzzetti (2009), Landslide rupture and the probability distribution of mobilized debris volumes, *J. Geophys. Res.*, *114*(F2), 2003–2012, doi:10.1029/2008JF001080.
Stark, C. P., and N. Hovius (2001), The characterization of landslide size distribution, *Water Resour. Res.*, *28*, 1091–1094.
Stock, J. D., and W. E. Dietrich (2003), Valley incision by debris flows: Evidence of a topographic signature, *Water Resour. Res.*, *39*(4), 1089, doi:10.1029/2001WR001057.
Swanston, D. N. (1970), Mechanics of debris avalanching in shallow till soils of southeast Alaska, Res. Pap., Pacific Northwestern Forest and Range Experiment Station, (PNW-103).
Tarolli, P., and D. G. Tarboton (2006), A new method for determination of most likely landslide initiation points and the evaluation of digital terrain model scale in terrain stability mapping, *Hydrol. Earth Syst. Sci. Discuss.*, *10*(5), 663–677.
Torres, R., W. E. Dietrich, D. R. Montgomery, S. P. Anderson, and K. Loague (1998), Unsaturated zone processes and the hydrologic response of a steep, unchanneled catchment, *Water Resour. Res.*, *34*(8), 1865–1879, doi:10.1029/98WR01140.
Van Rijsbergen, C. J. (1979), *Information Retrieval*, 2nd ed., Butterworths, London.
Van Westen, C. J., T. W. Van Asch, and R. Soeters (2006), Landslide hazard and risk zonation—Why is it still so difficult?, *Bull. Eng. Geol. Environ.*, *65*(2), 167–184.
Von Ruette, J., P. Lehmann, and D. Or (2013), Rainfall-triggered shallow landslides at catchment scale: Threshold mechanics-based modeling for abruptness and localization, *Water Resour. Res.*, *49*, 6266–6285, doi:10.1002/wrcr.20418.
Wieczorek, G. F. (1987), Effect of rainfall intensity and duration on debris flows in central Santa Cruz Mountains, California, *Rev. Eng. Geol.*, *7*, 93–104.
Wieczorek, G. F., and T. Glade (2005), Climatic factors influencing occurrence of debris flows, in *Debris-Flow Hazards and Related Phenomena*, pp. 325–362, Springer, Berlin.
Wilson, C. J., W. E. Dietrich, and T. N. Narasimhan (1989), Predicting high pore pressures and saturation overland flow in unchannelled hillslope valleys, paper presented at Hydrology and Water Resources Symposium, Inst. of Eng., Christchurch, New Zealand.
Wilson, R. C., and G. F. Wieczorek (1995), Rainfall thresholds for the initiation of debris flows at La Honda, California, *Environ. Eng. Geosci.*, *1*(1), 11–27.
Wu, T. H., W. P. McKinnell III, and D. N. Swanston (1979), Strength of tree roots and landslides on Prince of Wales Island, Alaska, *Can. Geotech. J.*, *16*, 19–33.
Wu, T. H., P. E. Beal, and C. Lan (1988), In-situ shear test of soil-root systems, *J. Geotech. Eng., ASCE*, *114*, 1376–1394.
Wu, W., and R. C. Sidle (1995), A distributed slope stability model for steep forested basins, *Water Resour. Res.*, *31*(8), 2097–2110, doi:10.1029/95WR01136.
Xie, M., T. Esaki, G. Zhou, and Y. Mitani (2003), Geographic information systems-based three-dimensional critical slope stability analysis and landslide hazard assessment, *J. Geotech. Geoenviron. Eng.*, *129*(12), 1109–1118.
Zhang, W., and D. R. Montgomery (1994), Digital elevation model grid size, landscape representation, and hydrologic simulations, *Water Resour. Res.*, *30*(4), 1019–1028, doi:10.1029/93WR03553.